Chemical Vapor Deposition of Organosilicon Composite Thin Films for Porous Low-k Dielectrics

by

April Denise Ross

M.S. in Chemical Engineering Practice
Massachusetts Institute of Technology, 2001

B.S. in Chemical Engineering
The University of Virginia, 1999

Submitted to the Department of Chemical Engineering
in Partial Fulfillment of the Requirements for the Degree of

DOCTOR OF PHILOSOPHY IN CHEMICAL ENGINEERING
AT THE
MASSACHUSETTS INSTITUTE OF TECHNOLOGY

January 2005
[February 2005]

© 2005 Massachusetts Institute of Technology. All rights reserved.

Signature of Author ....
Department of Chemical Engineering
January 19, 2005

Certified by ....
Karen K. Gleason
Professor of Chemical Engineering
Thesis Supervisor

Accepted by ....
Daniel Blankschtein
Professor of Chemical Engineering
Chairman, Committee for Graduate Students

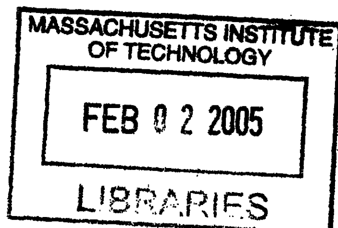

ARCHIVES

Chemical Vapor Deposition of Organosilicon Composite Thin Films for Porous Low-k Dielectrics

By

April Denise Ross

Submitted to the Department of Chemical Engineering
on January 19, 2005 in Partial Fulfillment of the
Requirements for the Degree of
Doctor of Philosophy in Chemical Engineering

ABSTRACT

Pulsed plasma enhanced chemical vapor deposition has produced organosilicon thin films with the potential use as low dielectric constant interconnect materials in microelectronic circuits. Both diethylsilane and octamethylcyclotetrasiloxane precursors were used, with oxygen and hydrogen peroxides oxidants respectively, to deposit low-k organosilicon films. FTIR, nanoindentation, ellipsometry, and dielectric constant measurements were demonstrated as a valuable film characterization tools to understand structure-property-processing fundamentals by quantifying structural bonding environments and relating those to the film properties. Nanocomposites were also produced using two novel techniques. First, crystal colloidal templates of polystyrene nanospheres were fabricated using evaporation-induced self-assembly. OSG was then deposited throughout the templates to create composite materials. Subsequently the polystyrene was removed upon thermal annealing to create highly porous OSG thin films. Second, ultrasonic atomization was used to deliver particles into a vacuum chamber during plasma-enhanced CVD of the organosilicon matrix to create composite thin films using an all-CVD technique. This process could extend CVD to applications currently only possible using wet processing techniques or multi-step processing.

Thesis Supervisor: Karen K. Gleason
Title: Professor of Chemical Engineering

To Mom and Dad

Acknowledgements

Though many days were spent envisioning this moment, it now surpasses my imaginable expectations, and that is due to the countless people that I owe greatly for their friendship, support, advice and guidance throughout this endeavor.

To my advisor, Karen, for being an inspiring and patient mentor as well as a never-failing source of ideas and enthusiasm throughout all stages of my work. Your direction and unwavering support provided an exceptional learning environment and resulted in a thesis of which I am proud.

To my thesis committee members, Professors Paula Hammond and Herb Sawin, who generously gave their time, offered their insights, and shared their expertise.

During this time, I have had the opportunity to work alongside a truly diverse and talented group of individuals. To members of the Gleason group, past and present, I could not have asked for a more wonderful group of people from whom I have learned so much. Each of you have uniquely contributed to my work and my life. Special thanks to the members of "team low-k." Dan, for generously giving your guidance and sharing your experience, Tom, for always listening and providing conference entertainment, and Kelvin, for continually fixing my computer, always taking the time to lend a hand, and reminding me that everything will work out.

The companionship of many friends has provided my life balance over the past five and a half years. To Christy and Ley, my constant and caring friends, who have been the instigators of many good times and a source of strength during the rough times. To Ian, Jim, Kevin, Kim, and Patty, my lunch crew, who provided me with daily mental health breaks filled with amusing distractions and entertaining conversations. Many additional thanks to those who enriched the quality of my life - Andrea, Anish, John, Kelvin, LaRuth, Martin, Murray, Scott, Todd, and Tom.

Most especially, to my parents, who instilled in me the importance and value of learning. Your selfless love and support never failed and is the foundation for all I have done and the inspiration for all I might achieve. No words can fully express my gratitude.

TABLE OF CONTENTS

Abstract	2
Dedication	3
Acknowledgments	4
List of Figures	8
List of Tables	12
List of Notations	13

CHAPTER ONE ______________________________ 14

Introduction

1.1	Motivation	15
1.2	Low k Materials	18
1.3	Chemical Vapor Deposition	22
1.4	Scope of Thesis	25
	References	28

CHAPTER TWO ______________________________ 30

Enhancement of mechanical properties of organosilicon thin films deposited from diethylsilane

	Abstract	31
2.1	Introduction	32
2.2	Experimental	33
2.3	FTIR and Structure Analysis	35
2.4	Optical and Mechanical Properties	38
2.5	Effect of Processing Conditions	40
	2.5.1 Flow Rate Ratios	40
	2.5.2 Plasma Processing Conditions	41
2.6	Conclusions	43
	References	46

CHAPTER THREE 48

Effects of condensation reactions on the structural, mechanical, and electrical properties of plasma-deposited organosilicon thin films from octamethylcyclotetrasiloxane

Abstract 49
3.1 Introduction 50
3.2 Experimental 52
3.3 FTIR and Structure Analysis 53
3.4 Mechanical Properties 58
3.5 Electrical Properties 63
3.6 Conclusions 64
References 66

CHAPTER FOUR 68

Nanoporous Organosilicate Glass Films via Chemical Vapor Deposition onto Colloidal Crystal Templates

Abstract 69
4.1 Introduction 70
4.2 Experimental 72
4.2.1 Formation of Templates 72
4.2.2 Pulsed-Plasma Enhanced Chemical Vapor Deposition 73
4.2.3 Characterization Methods 74
4.3 Optical and Mechanical Properties 75
4.4 Conclusions 83
References 84

CHAPTER FIVE 86

Chemical Vapor Deposited nanocomposites Fabricated Via Ultrasonic Atomization

Abstract 87
5.1 Introduction 88
5.2 Experimental 90
5.3 Results and Discussion 93
5.4 Conclusions 103
References 106

CHAPTER SIX ____ 108

Conclusions & Future Directions

6.1 Conclusions 109
6.1.1 OSG Matrix Materials 109
6.1.2 Composite Materials 110
6.2 Future Directions 112

APPENDIX A ____ 113

Reactor Configurations

List of Figures

CHAPTER ONE

Figure 1-1: Schematic representation of relevant physical dimensions for the RC delay.

Figure 1-2: Dielectric constant for varying degrees of porosity.

Figure 1-3: Characteristic diffusion times for small molecules.

Figure 1-4: Schematic of typical PECVD vacuum reactor.

CHAPTER TWO

Figure 2-1: FTIR Spectra of a film as-deposited (solid line) and annealed (dashed line).

Figure 2-2: FTIR Spectra of a film as-deposited and annealed, highlighting the silanol bonding region.

Figure 2-3: Displacement into surface versus hardness plot for as-deposited (open markers) and annealed (solid markers) films, with significant increase seen upon annealing.

Figure 2-4: Displacement into surface versus elastic modulus plot for as-deposited and annealed films, with significant increase seen upon annealing.

Figure 2-6: Effect of precursor flow rate ratios on hardness.

Figure 2-7: Effect of precursor flow rate ratios on elastic modulus.

Figure 2-8: Refractive indices and deposition rates versus plasma pulsing conditions.

CHAPTER THREE

Figure 3-1: FTIR Spectra of films as-deposited at varying oxidant flow rates. (b) expansion of hydroxyl bonding region (c) expansion of Si-$(CH_3)_x$ bonding region.

Figure 3-2: Effect of oxidant flow rate on ratio of T groups to D groups, determined by spectral curve fitting.

Figure 3-3: FTIR Spectra of a film as-deposited (solid line) and annealed (dashed line). (b) expansion of hydroxyl bonding region (c) expansion of Si-$(CH_3)_x$ bonding region.

Figure 3-4: Displacement into surface versus hardness plot for as-deposited (open markers) and annealed (solid markers) films, with significant increase seen upon annealing.

Figure 3-5: Displacement into surface versus elastic modulus plot for as-deposited and annealed films, with increase seen upon annealing.

Figure 3-6: Effect of oxidant flow rate on hardness and elastic modulus.

Figure 3-7: Hardness versus connectivity number.

Figure 3-8: Effect of oxidant flow rate and annealing on the dielectric constant.

CHAPTER FOUR

Figure 4-1: Schematic of self-assembly of a colloidal crystal template.

Figure 4-2: SEM images of a five-layer polystyrene template assembled on Si wafer from 96 nm polystyrene nanospheres : (a) Top view; (b) Oblique view.

Figure 4-3: FTIR spectra of (a) the template polystyrene nanospheres; (b) the composite film consisting of the template of polystyrene nanospheres filled with CVD OSG and (c) porous OSG film resulting from the decomposition of the polymer beads upon annealing.

Figure 4-4: AFM of composite materials with OSG deposition rates of (a) 45.8 nm/min and (b)72.0 nm/min.

Figure 4-5: Images of porous structures (a) SEM images of nanoporous OSG using 96nm bead template (b) TEM image of nanoporous OSG film using the 15nm bead template.

Figure 4-6: Plots of (a) the refractive index versus template percentage and (b) the dielectric constant versus template percentage.

CHAPTER FIVE

Figure 5-1: Reactor configuration of simultaneous plasma-enhanced deposition of matrix material and ultrasonic atomization deposition of particles.

Figure 5-2: Fluorescent microscopy of composite thin films consisting of OSG matrix and fluorescently labeled dextran particles.

Figure 5-3: FTIR spectra of (a) pure fluorescently labeled dextran (b) pure OSG matrix material and (c) the composite material.

Figure 5-4: Fluorescent microscopy of composite OSG films with labeled dextran where the later was delivered by ultrasonic atomization from aqueous solutions of varying ethylene glycol content (a) 100% (b) 95% (c) 90% and (d) 80% ethylene glycol. The volatility of the solvent greatly effects the particle deposition. The pure ethylene glycol has a comparatively low volatility, and does not evaporate before striking the substrate. Water, with a much higher volatility, evaporates quickly leaving only the dextran crystals to descend onto the substrate.

Figure 5-5: Calculated effect of reactor pressure on the droplet lifetime of ethylene glycol.

Figure 5-6: Fluorescent microscopy of OSG films with labeled dextran where the ultrasonic atomization of the dextran employed 100% ethylene glycol at (a) 150mTorr and (b) 500 mTorr. The evaporation driving force is fueled by the difference in the solvent saturation pressure and reactor pressure, and as the reactor pressure increases to 500 mTorr and approaches the saturation pressure, no solvent evaporation occurs and the droplets strike the substrate with their original diameter of 45 μm.

Figure 5-7: FTIR spectra of annealed composite thin film and (inset) fluorescent microscopy of annealed films. Both indicate removal of dextran particles.

Figure 5-8: SEM image of porous OSG matrix structure with 96nm pores, originally a composite film with polystyrene microbeads.

APPENDIX A

Figure A-1: Basic reactor configuration accommodating an ultrasonic atomizer.

Figure A-2: Basic reactor configuration accommodating an ultrasonic atomizer, overhead view.

Figure A-3: CAD drawing of redesigned reactor lid accommodating ultrasonic atomizer (top view).

Figure A-4: CAD drawing of redesigned reactor lid accommodating ultrasonic atomizer (side view).

Figure A-5: Detailed drawing of redesigned showerhead accommodating ultrasonic atomizer.

List of Tables

CHAPTER ONE

Table 1-1: Levels of metallization

Table 1-2: SIA Roadmap indicating demand for low-k technology

Table 1-3: Polarizability of common bonds

CHAPTER THREE

Table 3-1: Structural composition percentages from FTIR and connectivity numbers

CHAPTER FIVE

Table 5-1: Effect of solvent on evaporation rate of droplets

List of Acronyms, Abbreviations, and Symbols

A	Absorbance
C	Capacitance
CMP	Chemical Mechanical Polishing
CRN	Continuous Random Network
CVD	Chemical Vapor Deposition
CW	Continuous Wave
d	Film Thickness
DES	Diethylsilane
d_p	Droplet Diameter
D_v	Diffusion Coefficient of Solvent
D_4	Octamethylcyclotetrasiloxane
E	Elastic Modulus
EG	Ethylene Glycol
ε_0	Vacuum Permittivity
ESH	Environment, Safety and Health
f	Frequency
FTIR	Fourier Transform Infrared Spectroscopy
GPa	Gigapascals
H	Hardness
I	Mass Rate of Evaporation
ITRS	International Technology Roadmap for Semiconductors
ITS	Interferometry for Thermal Stability
k	Dielectric Constant
n	Index of Refraction
MSE	Mean Squared Error
M, MW	Molecular Weight
P	Power
PECVD	Plasma-Enhanced Chemical Vapor Deposition
p_d	Partial Pressure at the Droplet's Surface
PLD	Pulsed Laser Deposition
PPECVD	Pulsed Plasma-Enhanced Chemical Vapor Deposition
p_∞	Partial Pressure of Solvent in the Reactor
R	Resistance
R	Gas Constant
RF	Radio Frequency
<r>	Average Connectivity Number
ρ_p	Density of the Drop Liquid
sccm	Standard Cubic Centimeters per Minute
SiCOH	Organosiloxane / Carbon Doped Oxide
t	Droplet Lifetime
T	Temperature
TEOS	Tetraethoxysilane
VASE	Variable Angle Spectroscopic Ellipsometry

CHAPTER ONE

INTRODUCTION

1.1 MOTIVATION

The demand for high-speed devices in today's electronics is surging and several changes are being investigated for improvement of current devices. At the forefront of these options is reducing the resistance, R, of the wire interconnects and reducing the capacitance, C, between the wires.[1] Reducing the wire resistance is especially important as chip and wire size decreases, since the resistance is inversely proportional to the cross sectional area of the wire.[1] Since 1965, Moore's Law, which states that the number of transistors on a computer chip doubles roughly every eighteen months, has compelled the drive for miniaturization.[2] One option recently implemented involved substituting copper for the standard aluminum metallization with tungsten plugs. Copper offers both a lower resistivity, 1.7 μΩ-cm compared to 3.0 μΩ-cm, and improved electro-migration resistance.[1] Transistor speed can be quantified by the RC delay, which is the intrinsic time delay for signal propagation, and is given in the equation below

$$\tau = RC = \left(\frac{\rho L_m}{W_m T_m}\right) * \left(\frac{k\varepsilon_o W_m L_m}{T_d}\right) = \frac{k\varepsilon_o \rho L_m^2}{T_d T_m} \qquad 1\text{-}1$$

Figure 1-1 depicts the relative physical dimensions referred to in equation 1-1. Holding all dimensions constant, only the metal resistivity, ρ, and the dielectric constant, k, can be manipulated. By lowering the resistivity of the metal the RC delay time, τ, is decreased proportionally.

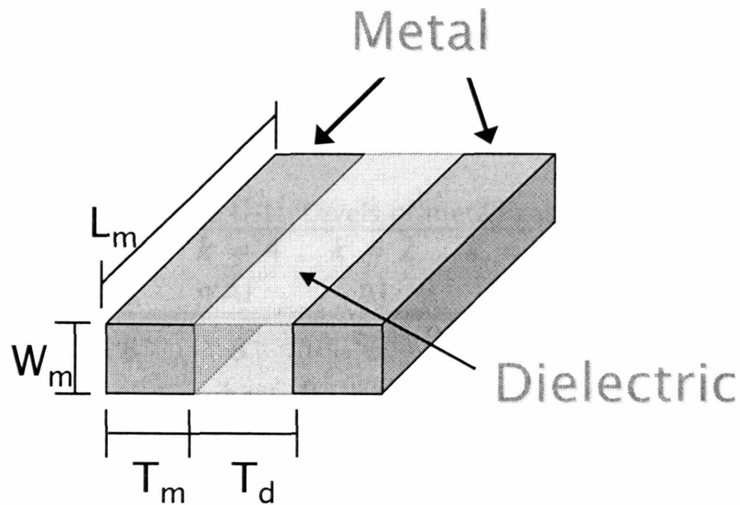

Figure 1-1: Schematic representation of relevant physical dimensions for the RC delay.

Reducing the dielectric constant, and thereby the capacitance, of the interlevel material is another viable option for reduction of the RC delay. In addition, this change can also reduce power consumption, P, which is particularly important in small, portable devices, and cross talk noise, N, between adjacent metal lines.

$$P \propto CV^2 f \tag{1-2}$$

$$N \sim \frac{C_{line-to-line}}{C_{total}} \tag{1-3}$$

Therefore, by choosing to decrease the dielectric constant, the designer is afforded a higher degree of freedom.[3] Another driving force for lower metal resistivity and dielectric capacitance is that fewer levels of metallization are required for a fixed degree of functionality, as shown in Table 1-1. Fewer metal

layers lead to less materials, less energy, and less waste as well as decreased device complexity.[1]

Table 1-1: Levels of metallization

CD (μm)	$k = 4$ Al	$k = 2$ Al	$k = 4$ Cu	$k = 2$ Cu
0.18	8	6	6	4
0.1	14	11	11	7

Once realized, the integration of theses new low-k materials into current device construction has proved to be an additional challenge for manufacturers. The ITRS Roadmap, which outlines where the technological requirements for the semiconductor industry, illustrates these difficulties, as the expectations for dielectric constant reduction has been notably delayed between 2001 and 2003, as shown below in Table 1-2.[3] In year 2007 at the 65nm technology node, the 2001 projection indicated an effective dielectric constant of 2.3 to 2.7 would be mandated. In the two years before the 2003 roadmap publication, significant difficulties had been encountered to cause that value to increase to 2.7 to 3.0. At the time of publication, solutions for these values were still unknown.

Table 1-2: SIA Roadmap indicating demand for low-k technology

Year	2001	2003	2004	2007	2010	2013	2017
Technology Node	130	130	90	65	45	32	22
2001 ITRS Roadmap	3.0-3.6	3.0-3.6	2.6-3.1	2.3-2.7	2.1	1.9	1.8
2003 ITRS Roadmap		3.3-3.6	3.1-3.6	2.7-3.0	2.3-2.6	2.0-2.4	2.0

1.2 Low-k Materials

Two different pathways can be explored, independently or together, to lower the *k*-value relative to SiO_2 (k~4), once the industry standard. Both incorporating atoms and bonds that have a lower polarizability and decreasing the density of the material reduce the dielectric constant. Both of these avenues can be related to the overall polarization, P, of the material. All matter is made of electrically charged particles, electrons and nuclei combining to form atoms, molecules, and ions.[4] When brought into an external electric field (E), the forces acting upon the charges bring about a small displacement of the electrons relative to the nuclei. Polarization is the acquired dipole moment per unit volume in response to an applied electric field. The dielectric constant can be related to the polarizability by the following equation.

$$k = 1 + \frac{4\pi P}{E} \tag{1-4}$$

The dielectric constant is dependent on temperature, density or pressure, and chemical composition. Polarization includes three parts arising from the electronic, atomic and orientation responses of the material, each corresponding with the motions of a different kind of microscopic particles with different characteristic times.[4,5] At high frequencies, the electronic response dominates and the dielectric constant equals the square of the optical index of refraction, $k = \eta^2$.

Table 1-3 shows some typical polarizabilities of common bonds.[5] This indicates that single bonds, particularly C-C, C-F, and C-O, have the lowest polarizabilities, as double bonds have increased mobility of the π electrons. Therefore, two important classes of low-*k* materials are carbon-doped silicon

oxides, or organosilicate glasses (OSGs) and fluorinated hydrocarbons. OSG have two main advantages. The Si-C bonds are more covalent in nature than the Si-O bonds, since Si and O have a large electronegativity difference giving ionic character to their bond and increasing polarizability. Also by adding methyl (-CH_3) groups bound to Si atoms, a proportion of the Si-O bonds are terminated resulting in a "loosening" of the lattice as lighter C and H atoms replace the densely packed Si and O crosslinked network; therefore, a reduction in the film density and dielectric constant is achieved.[5,6]

Table 1-3: Polarizability of common bonds

Bond	Polarizability ($Å^3$)
C-C	0.531
C-F	0.555
C-O	0.584
C-H	0.652
O-H	0.706
C=O	1.02
C=C	1.643

Current dense OSG films have dielectric constants ranging from 2.7 to 3.3.[7-19] Another method of loosening the lattice involves the addition of fluorine into the film. Fluorine atoms exhibit particularly high electronegativity, which facilitates tight binding of electrons and decreased polarizability.[5] However, fluorine addition can also degrade the stability of the film.[3,20]

The introduction of void space, which has a *k*-value of 1.0, the theoretical lower limit for *k*, is another approach for the reduction of dielectric constants in thin films. Voids can be introduced into the materials through air bridge fabrication or by creating nano-porous films. Many of these film's properties depend on the degree of porosity, p, where the air bridge would have the highest porosity of 1. There are many models that predict the effective dielectric constant

for heterogeneous mixtures.[4] The Rayleigh model assumes the pores are a uniform distribution of spheres in a cubic lattice, while the Looyenga model assumes spheres of mixed composition. Figure 1-2 depicts how the dielectric constant changes with degree of porosity for these models for both silicon dioxide and a typical OSG with fully dense dielectric constant of 2.7.

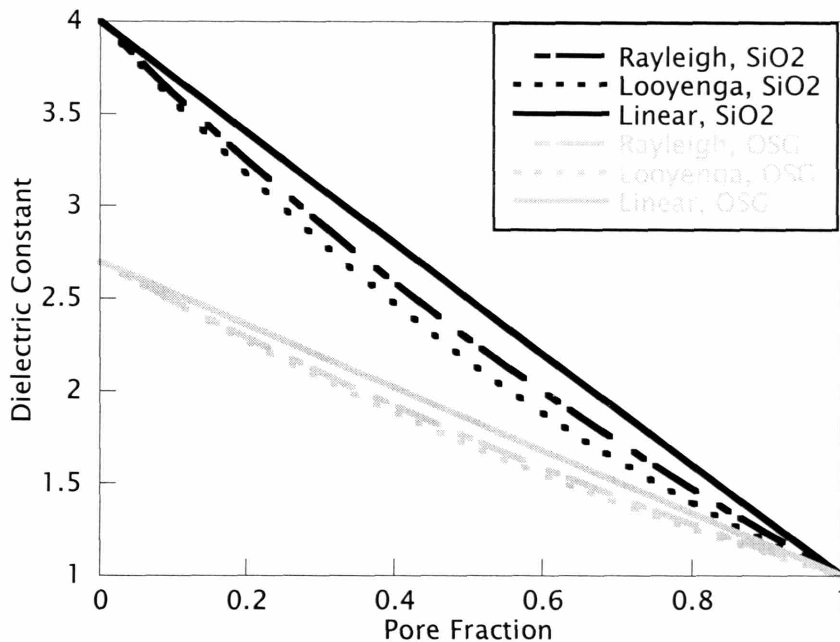

Figure 1-2: Dielectric constant for varying degrees of porosity.

It is clear from this graph that porosity plays a secondary role to matrix material in lowering the dielectric constant. While ample research continues to investigate reducing the dielectric constant of dense OSG materials further, their extension to ultra-low dielectric constant application is limited by material properties. In order to meet all of ITRS requirements outlined in Table 1-2, porosity will eventually be necessitated. Although increased porosity is favorable for the dielectric constant, the film has other characteristics that suffer as porosity is increased. Mechanical strength is reduced with porosity, p, by $(1-p)^3$ while thermal conductivity is reduced by $(1-p)^{1.5}$.[5]

With current feature size in the 100 nm range, it is imperative that the pore size remains below 10nm and have a small distribution. Any pores larger than 10 nm could be considered defects and can affect mechanical strength. Currently under debate is whether the pores should be open or closed on a microstructural level. Open pores are connected throughout the film and occur at porosities greater than approximately 30%. Some believe the closed pore structure is better as it would help relieve low-k voiding, which occurs when fluorinated etch gas used in later processing step permeates into the voids. If then annealed, the pores can coalescence, forming macroscopic voids.[21,22] The idea behind closed pore structures is that it would prevent the diffusion of the etch gas into the pores. However, when dealing with small molecules such as fluorine at typical processing temperatures (400°C) the characteristic diffusion times through silicon dioxide are short, indicating that the etch gas would diffuse into the pores whether open or closed. Figure 1-3 shows the characteristic diffusion times through varying depths of silicon dioxide for other small molecules as a function of temperature. Additionally, an OSG matrix would be significantly less dense allowing even faster diffusion of molecules through the film.

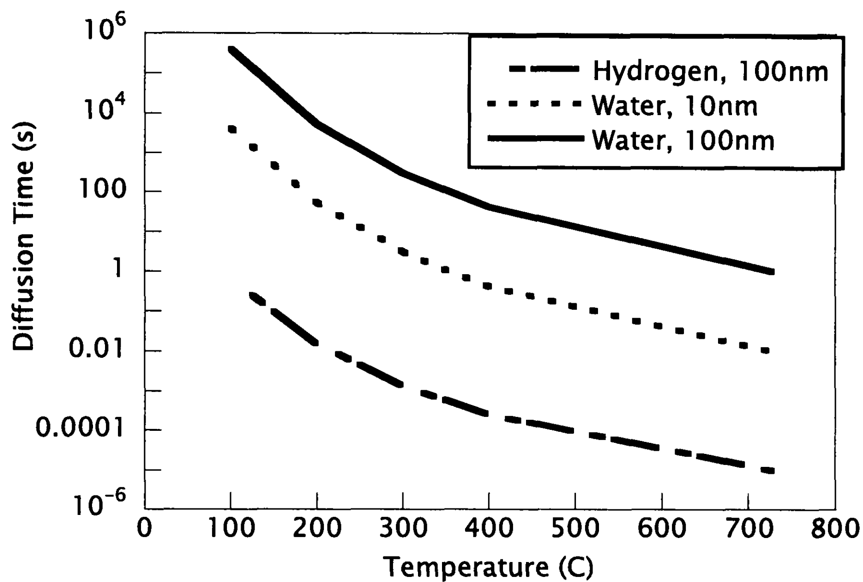

Figure 1-3: Characteristic Diffusion Times for small molecules

Throughout these processing steps, it is important that the film maintain certain properties essential for any low-k film; these properties include thickness, uniformity, refractive index, adhesion, chemical resistance, thermal stability, pore size and distribution, coefficient of thermal expansion, glass transition temperature, film stress, and value of the diffusion coefficient for copper.[23]

1.3 Chemical Vapor Deposition

Several different methods are routinely used for depositing low-*k* materials. The main dichotomy is between spin-on dielectric (SOD) and chemical vapor deposition (CVD), each with its advantages and disadvantages. Manufacturers of spin-on materials claim better extendibility to future generations because of the demonstrated ability to add pores, especially in the sub-2.5 range when porous low-k material will be required. These materials begin as a dense blend of two substances, one of which is later decomposed to create the porous structure. This type of hybrid system is referred to as a matrix-porogen composite. Thus far, SOD

has demonstrated higher capabilities to produce porous low-k materials using this technique.[14,23-26] Yang et. al. has produced porous thin films using cyclic silsesquioxane as the matrix material and thermally labile cyclodextrin molecules as the porogen, with resulting dielectric constants as low as 1.9. However, SOD has several drawbacks, primarily from an environmental, health, and safely viewpoint. It requires the use of a solvent to distribute the polymers and often a subsequent rinsing step, both of which have significant waste and can expose workers to chemicals and out-gassing. Additionally, wet processes are often limited by the solubility of polymers and problems can occur when fabricating composite materials with the aggregation of particles.

On the other hand, CVD manufacturers claim more reuse of existing toolsets and simpler integration due to silicon dioxide-like structure of CVD siloxanes.[23] CVD processes excel at producing thin, conformal coatings with low levels of contaminants when high purity precursors are used. Chemical vapor deposition is a more environmentally friendly manufacturing method that utilizes gas phase chemistries in a low to ultra-low pressure environment to produce well-defined, high quality films in a controllable and tunable fashion.[27] CVD involves several steps: creation of reactive species in the gas phase, transport to the substrate surface, adsorption of onto the surface, diffusion on the surface, polymerization and film growth, and desorption of volatile, non-polymerized species.[28] Furthermore, vacuum techniques such as CVD have limited worker chemical exposure and no waste solution.

Plasma-enhanced CVD (PECVD) occurs when a low-density plasma is generated by radio frequency excitation of the precursor gas. The plasmas are composed of ions, radicals, and excited neutrals from the gas that react on a temperature-controlled substrate to form a film.[27] A typical PECVD reactor is depicted in Figure 1-4.

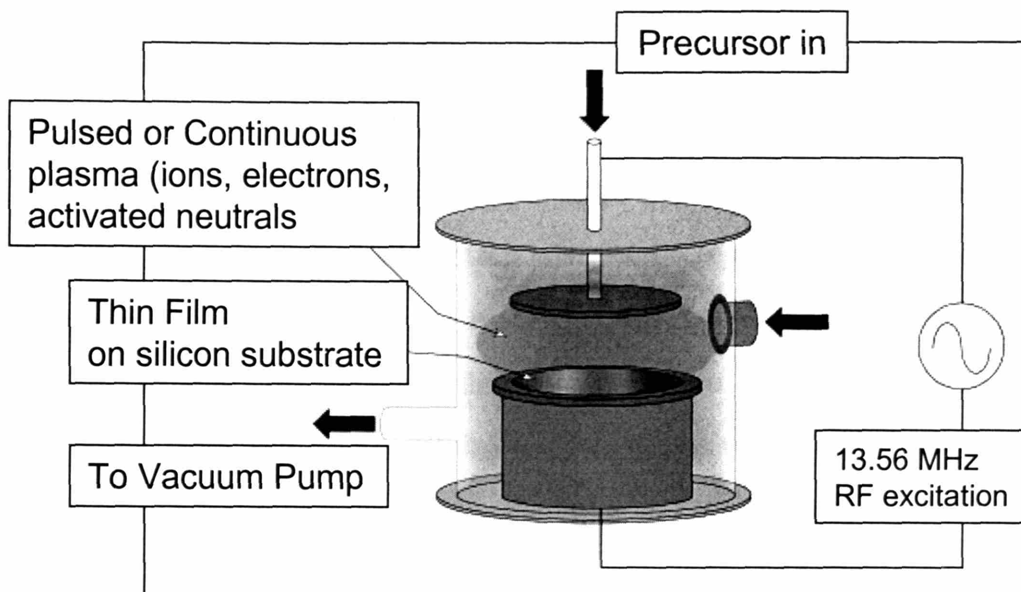

Figure 1-4: Schematic of typical PECVD vacuum reactor

Continuous wave plasmas are commonly used and occur when a constant electric field is applied for the entire duration of the deposition. At higher powers, the precursor molecules undergo more fragmentation which produces highly crosslinked films bearing little resemblance to the original precursor structure. Additionally, at high powers, polymerization often begins in the gaseous phase, leading to unwanted particle generation.[29] The polymers also tend to show aging effects upon exposure to the atmosphere as well as a higher number of free radicals or dangling bond due to ion bombardment.

Alternatively, pulsed plasma-enhanced CVD (PPECVD) occurs when the electric field is turned on and off in a distinct pattern, with times in the millisecond range. The equivalent power is calculated by multiplying the duty cycle, which is the percent of time the plasma is on, by the peak power of the plasma. For example, a 10 ms - 40 ms on-ff pulse cycle with a 300 watt peak power would be equivalent to a 60 W average continuous plasma. Beyond diminishing the powder

effects and reducing the number of dangling bonds, PPECVD also provides another parameter with which to further fine tune the properties of the thin films.

The semiconductor industry has struggled with determining an all CVD approach to creating porous, low-*k* materials. Most research in this area focuses on simultaneously co-depositing the matrix, normally silicon dioxide based, and the porogen, usually an organic species, from two or more precursors.[30-32] Problems occur from the compatibility of the deposition conditions needed to produce two very different polymers simultaneously.

1.4 Scope of Thesis

This thesis investigates OSG thin films deposited by PPECVD, studying the structure-property-processing relationship, and establishes an all-CVD approach to creating matrix-porgen composites using a novel manufacturing technique. It is structured into four main technical chapters, each a published journal article and as such can be read as self contained works.

CHAPTER TWO reports on the plasma polymerization of OSG thin films deposited from diethylsilane and oxygen precursors. The additional organic content of diethylsilane compared to traditional methyl-doped precursors was selected to increase the carbon content in the film, which is known to improve electrical properties. Changes in mechanical properties observed with annealing were placed in context of reactions occurring between proximal end groups.

CHAPTER THREE presents results from organosilicon thin films deposited from octamethylcyclotetrasiloxane and hydrogen peroxide using pulsed-plasma enhanced chemical vapor deposition. Hydrogen peroxide was used as an oxidant to promote hydroxyl incorporation into the film structure. Annealing generated condensation reaction throughout the film, altering its composition and properties.

FTIR analysis was used to link the film structure with its electrical and mechanical properties and the work was placed within the framework of the percolation of rigidity.

CHAPTER FOUR establishes a two-step technique for the fabrication of porous OSG materials. Evaporation-induced self-assembly was used to create templated polystyrene microbead arrays of well-defined and controllable thicknesses. PPECVD was used to deposit a matrix OSG from silane precursors in and throughout the bead template. Subsequent annealing decomposes the polystyrene to form a porous OSG thin film.

However, this process is unable vary the degree of porosity and is comprised of multiple steps, including a wet process. The process was modified slightly using a layering technique, whereby layers of polystyrene beads are alternated with OSG deposition. While this adjustment offers improved control over percent porosity, it adds extra steps and increases the complexity of the process.

CHAPTER FIVE introduces a novel technique implement to create composite thin films with an all-CVD process. Films were fabricated by employing ultrasonic atomization to introduce the porogen particles into the vacuum chamber during plasma-enhanced deposition of a matrix material. Fluorescently labeled dextran particles were employed to allow direct observation of the dextran within the matrix film. Particle deposition was explored in the context of solvent properties as well as reactor conditions. This process could extend the CVD technique to applications for composite materials currently only feasible using wet processing techniques or multi-step processing.

CHAPTER SIX presents some concluding thoughts about the work and comments on possible further directions that this research might take, based on the results presented.

This work would not have been possible without the generous support of the NSF/SRC Engineering Research Center of Environmentally Benign Semiconductor Manufacturingand the SRC / Texas Instruments for their support through the Graduate Fellowship Program.

References

1. M. T. Bohr, *Solid State Technol.* **39**, 105 (1996).
2. G. E. Moore, *Electronics* **38**, 1 (1968).
3. M. B. Anand, M. Yamada, and H. Shibata, *IEEE Trans. Electron Devices* **44**, 1965 (1997).
4. C. J. F. Böttcher, O. C. van Belle, P. Bordewijk, and A. Rip, *Theory of Electric Polarization*, 2nd ed (Elsevier Scientific Pub. Co., New York, 1973).
5. M. Morgen, E. T. Ryan, C. H. Jie-Jua Hua, T. Cho, and P. S. Ho, *Annu. Rev. of Mater. Sci.* **30**, 645 (2000).
6. D. Thomas, Y. Song, and K. Powell, *Solid State Technol.* **44**, 107 (2001).
7. D. D. Burkey and K. K. Gleason, *J. Appl. Phys.* **93**, 5143 (2003).
8. D. D. Burkey and K. K. Gleason, *J. Electrochem. Soc.* **151**, F105 (2004).
9. A. Grill, *Thin Solid Films* **398**, 527 (2001).
10. A. Grill, V. Patel, and C. Jahnes, **145**, 1649 (1998).
11. A. Grill and V. Patel, *J. Appl. Phys.* **85**, 3314 (1999).
12. A. Grill and D. A. Neumayer, *J. Appl. Phys.* **94**, 6697 (2003).
13. C.-T. Lin, F. Li, and T. D. Mantei, *J. Vac. Sci. Technol. A* **17**, 735 (1999).
14. L. Peters, *Semiconductor International* (May 2002).
15. Q. G. Wu and K. K. Gleason, *Plasmas Polym.* **8**, 31 (2003).
16. Q. G. Wu and K. K. Gleason, *J. Vac. Sci. Technol. A* **21**, 388 (2003).
17. J. Widodo, W. Lu, S. G. Mhaisalkar, L. C. Hsia, P. Y. Tan, L. Shen, and K. Y. Zeng, *Thin Solid Films* **462-63**, 213 (2004).
18. E. S. Lopata, L. Young, and J. T. Felts, *Mater. Res. Soc. Symp. Proc.* **612**, D5.3.1 (2000).
19. M. J. Loboda, *Microelectron. Eng.* **50**, 15 (2000).
20. L. Peters, *Semiconductor International* (September 1998).
21. R. P. Mandal, D. Cheung, P. W.-M. Lee, and C.-I. Lang, USA Patent No. 207791 (August 22 2000).
22. R. P. Mandal, D. Cheung, and W.-F. Yas, USA Patent No. 177044 (January 9, 2001 2001).
23. L. Peters, *Semiconductor International* (June 2000).
24. A. T. Kohl, R. Mimna, R. Shick, L. Rhodes, Z. L. Wang, and P. A. Kohl, *Electrochem. Solid State Lett.* **2**, 77 (1999).

25. R. D. Miller, *Science* **286**, 421 (1999).
26. M. Gallagher, T. Adams, C. Allen, N. Annan, R. Blankenship, J. Calvert, W. Fillmore, R. Gore, D. Gronbeck, S. Ibbitson, C. Jehoul, A. Lamola, G. Prokopowicz, N. Pugliano, C. Sullivan, M. Talley, and Y. You, *Abstr. Pap. Am. Chem. Soc.* **224**, U510 (2002).
27. R. D'Agostino, *Plasma deposition, treatment, and etching of polymers* (Academic Press, Boston, 1990).
28. M. L. Hitchman and K. F. Jensen, *Chemical Vapor Deposition, Principles and Applications* (Academic Press, New York, 1993).
29. H. Yasuda, *Plasma Polymerization* (Academic Press, Inc., Orlando, 1985).
30. A. Grill and V. Patel, *Appl. Phys. Lett.* **79**, 803 (2001).
31. A. Grill, *J. Appl. Phys.* **93**, 1785 (2003).
32. D. D. Burkey and K. K. Gleason, *J. Vac. Sci. Technol. A* **22**, 61 (2004).

CHAPTER TWO

ENHANCEMENT OF MECHANICAL PROPERTIES OF ORGANOSILICON THIN FILMS DEPOSITED FROM DIETHYLSILANE

A. D. Ross and K. K. Gleason

ABSTRACT

Pulsed-plasma enhanced chemical vapor deposition was used to deposit organosilicon thin films from diethylsilane and oxygen. FTIR analysis shows significant organic content as well as hydroxyl and silanol moieties present in the as-deposited materials. FTIR showed a complete removal of hydroxyl groups after annealing at 400 °C for 1 hour. This indicates a condensation reaction between proximal hydroxyl groups leading to the formation of additional Si-O-Si linkages, which would increase the mechanical properties of the film. Mechanical property measurements were in accordance with this hypothesis, as both the hardness and modulus increased by over 50% after annealing. Film structure and properties were strongly dependent on the precursor feed ratio.

2.1 INTRODUCTION

The demand for high-performance electronic devices is surging, motivating research into improvements of interconnect speed. One of these options is reducing the capacitance, C, between the wires via the dielectric constant. This is not only a option for reduction of the RC delay, but can also reduce power consumption, P, and cross talk noise, N, between adjacent metal lines.[1] One important class of low-*k* materials is the carbon-doped silicon oxides, also known as organosilicate glasses (OSGs).[2,3] OSGs have two main advantages. First, the Si-C bonds are more covalent in nature than the Si-O bonds, since Si and O have a large electronegativity difference giving ionic character to their bonds leading to increased polarizability and hence higher dielectric constants.[4] Additionally, by adding organic content such as methyl ($-CH_3$) and ethyl ($-CH_2CH_3$) groups bound to Si atoms, a proportion of the Si-O bonds are terminated resulting in a "loosening" of the lattice as lighter C and H atoms replace the densely packed Si and O crosslinked network; therefore, a reduction in the film density and *k*-value is achieved.[3,4] Current research of dense OSG films has generated dielectric constants ranging from 2.4 to 3.3.[5-8] Improvement of mechanical properties is essential for successful integration of OSG films in advance microelectronic devices.[9]

The CVD OSG films have found wide acceptance in semiconductor manufacture.[10] CVD utilizes gas phase chemistries in a low to ultra-low pressure environment to produce well-defined, high quality films in a controllable and tunable fashion.[11] This work focuses on OSG thin films created from diethylsilane (DES) and oxygen. The DES precursor has previously been used to produce both SiO_2 and SiNCH thin films using a variety of methods for number of different application targets.[12-20] Silane precursors such as methylsilane, dimethylsilane and trimethylsilane have often been utilized to create OSG dielectric materials, and

dielectric constants for trimethylsilane (3MS) and O_2 have been shown in the range of 2.4 to 3.0 using PECVD.[7,21] However, these silanes are generally highly explosive and therefore present considerable health and safety hazards. DES is more environmentally benign precursor and is an evolutionary step toward achieving higher organic content through the addition of ethyl groups instead of methyl groups in OSG materials.

The addition of organics to the dielectric results in a more open structure, reducing density and network bonding, both of which contribute to reduced mechanical properties. This creates issues with latter processing steps, such as the ability to survive chemical-mechanical polishing.[2,9] Spin-on deposition, another technique sometimes used for low-k materials, relies on a thermal curing step that leads to a structural transformation which supplies the material's strength.[22-26] Often utilizing alcohol or water condensation chemistry, reactions between proximal end groups help to crosslink the film, thereby making it mechanically robust. In this work, the ability of condensation chemistry to improve the mechanical properties of CVD OSG films is explored.

2.2 EXPERIMENTAL

Depositions were carried out in a custom-built, parallel-plate vacuum chamber. The PECVD system has an upper electrode powered by a 13.56 MHz RF source (ENI HF650) with attached matching network (Heathkit SA2060-A) and a grounded lower electrode. The lower electrode also functions as the substrate stage and was kept at room temperature using a water cooled system. In addition, electrostatic clamping capabilities were utilized to help maintain constant substrate temperatures. The substrates used were 100 mm diameter silicon wafers. The upper electrode / shower-head distributes all incoming precursor gases over the

substrate. Diethylsilane (DES, Gelest Inc., CAS 542-91-6, > 95%) was the monomer used with no further purification. The DES was volatilized in a glass jar and delivered to the reactor chamber through a calibrated needle valve. Oxygen and argon were delivered to the reactor using a UNIT Instrument URS-100 Mass Flow controlling system. For all depositions, chamber pressure was maintained at approximately 300 mTorr and is controlled by a butterfly valve (MKS 253B) connected to an MKS model 651C exhaust valve controller. When investigating thermal stability, films were annealed at 400 °C and ambient pressure in a nitrogen atmosphere for one hour.

Fourier Transform Infrared (FTIR) Spectroscopy was performed on a Thermo Nicolet Nexus 870 ESP spectrometer in transmission mode at 4 cm^{-1} resolution using 64 scan averaging. A 10 minute nitrogen purge was performed between each measurement to diminish the effects of carbon dioxide and moisture. All spectra were baseline corrected and had their intensity normalized to a thickness of 5000 Å using their measured thicknesses and Beer's Law.

Film thicknesses and indices of refraction (n_{633}) were determined using VASE, Variable angle spectroscopic ellipsometry, performed on A Woolam M-2000 spectrometer having a xenon light source.. Data was acquired at three angles (65°, 70°, and 75°). The Cauchy model[27] was used to fit the data and the mean-squared errors (MSE) was low (<10), signifying a match between the model and the data. In addition to quantifying the optical properties, the refractive index also gives an indication of the electrical properties, as the square of the refractive index is the lower limit of the dielectric constant. This approximation is most appropriate in insulating materials having the smallest induced dipoles and takes into consideration only electronic polarization.[28,29] This measure will be used to gauge the electrical properties because dielectric constant measurements using a mercury probe can be error prone due to their high sensitivity to films thickness.

Mechanical properties were measured at the Novellus Research Center in Tualatin, Oregon. Measurements of hardness and elastic modulus were performed using a MTS Systems Nano-Indenter XP and MTS patented continuous stiffness measurement technique. With this technique, each indent gives hardness and elastic modulus as a continuous function of the indenter's displacement into the samples. The surface approach velocity was 5nm/s and the load versus displacement slop was -81.6 N/m. Experiments were terminated at a depth of approximately 300 nm. A Berkovick diamond tip was used in the measurements. The films were 1 μm or greater in thickness to minimize any substrate effects on the results. Fused silica was tested and used as a control sample.

2.3 FTIR AND STRUCTURE ANALYSIS

Figure 2-1 shows the FTIR spectra of film deposited from a mixture of DES and O_2, both as-deposited and after annealing. The deposition was carried out with flow rates of 7 sccm of DES, 20 sccm of O_2, and 6 sccm of argon using 10/70 ms on-time/ms off-time pulsed plasma excitation and 300W peak power. The assignments of the FTIR bands for OSG materials have been previously reported.[30] The peaks in the 3000 - 2850 cm^{-1} region correspond $-CH_3$ and $-CH_2$, revealing the significant presence of hydrocarbon content in the film. The definite presence of the $-CH_2$ peaks at 2920 and 2950 cm^{-1} indicates either the existence of intact ethyl groups or methylene bridging. The broad peak at 3700-3200 cm^{-1} shows considerable free -OH inclusion in the as-deposited film, most likely due to incorporation of impurities such as water and silanol moieties. Hydroxyl incorporation also appears around 920-830 cm^{-1}, signifying the stretch of the silanol (Si-OH) bond, as shown in Figure 2-2. Also located in this region of the spectrum is Si-C bond, which extends from 870 to 750 cm^{-1} for the $Si-CH_3$ rock

and from 975-945 cm^{-1} for Si-CH_2CH_3. The peaks between 2280 and 2080 cm^{-1} show the presence of Si-H in the films. The Si-O-Si backbone absorbance appears between 1000 and 1200 cm^{-1}, with the rightmost adsorption peak centered around 1060 cm^{-1}. This characteristic peak is associated with longer chain siloxanes. The broad shoulder to the left of this peak is indicative of a more complicated network structure. Si-$(CH_3)_x$ symmetric stretching bands occur between 1240-1300 cm^{-1}. However, this area is largely overshadowed by the broadened Si-O shoulder which encompasses Si-CH_2CH_3 at 1250-1220 cm^{-1} as well as Si-CH_2CH_2-Si at 1180-1120 cm^{-1}.

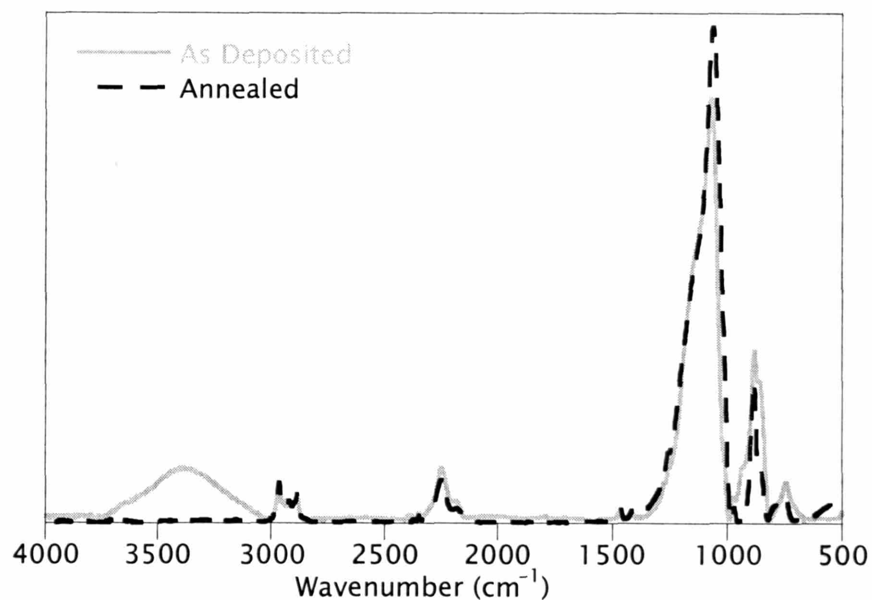

Figure 2-1: FTIR Spectra of a film as-deposited (solid line) and annealed (dashed line).

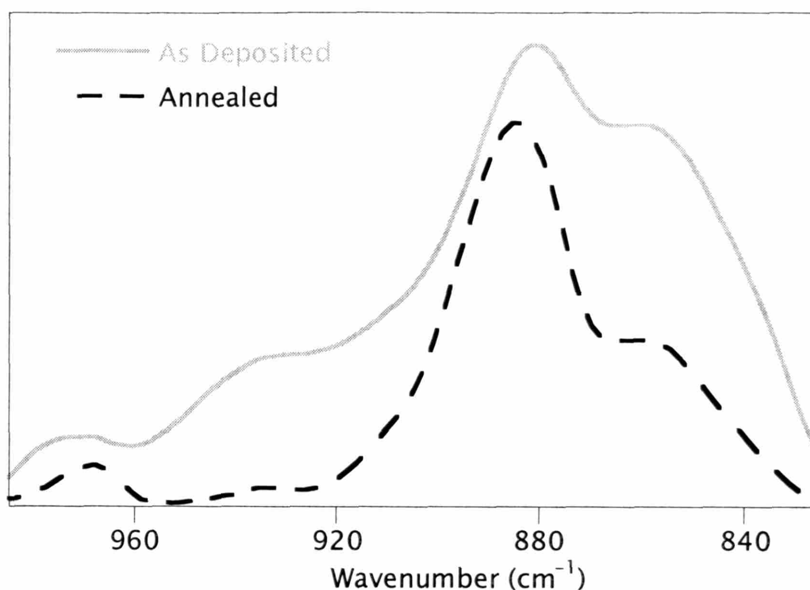

Figure 2-2: FTIR Spectra of a film as-deposited and annealed, highlighting the silanol bonding region.

After annealing, significant changes can be observed in the film structure. Most notably, the broad -OH peak at 3700-3200 cm^{-1} disappears, indicating complete removal of the hydroxyl group after annealing. Correspondingly, the peaks assigned to the silanol bond at 830 - 920 cm^{-1} show a significant decrease, particularly in the peak at 850 cm^{-1}, further implicating the removal of the silanol moieties. However, these peaks do not vanish completely as this region is filled with various other stretches. Another apparent difference is the increase in intensity of the Si-O-Si peak at 1060 cm^{-1}, indicating the formation of additional Si-O linkages. Combined, these two variances can be attributed to adjacent Si-OH groups undergoing a condensation reaction as outlined below.[31-33]

$$\sim Si\text{-}OH \;+\; HO\text{-}Si\sim \;\rightarrow\; \sim Si\text{-}O\text{-}Si\sim \;+\; H_2O\uparrow$$

This reaction facilitates the creation of additional Si-O networking resulting in a higher crosslinked film and improved mechanical strength.[30] In the absence of film shrinkage, the loss of water also decreases the overall density of the film.

2.4 Optical and Mechanical Properties

Both the optical and mechanical film properties were examined before and after annealing. Film thickness retention after annealing was >90% demonstrating reasonable thermal stability. The refractive index decreased from 1.442 to 1.430 after annealing, partially due to the loss of -OH from the film. Additionally, the reduction in film density brought about by the loss of water in the condensation reaction and increased crosslink formation would also contribute to a lower index of refraction.

Figure 2-3 shows the hardness versus displacement curves for the as-deposited and annealed films; Figure 2-4 shows modulus versus displacement.. For both hardness and modulus, a substantial increase is seen upon annealing. Hardness increased over 70% from 0.98 to 1.67 GPa, while the modulus jumped from 6.84 to 10.58 GPa, a 54% increase. This change is consistent with the condensation reaction creating a more crosslinked film, as confirmed by the FTIR analysis. These results strongly suggest that higher crosslinking leads to a more rigid, mechanically stable structure. Changes in mechanical properties as a result of crosslinking in OSG films induced during anneal have previously been reported, with hardness increasing between 1-20% and the modulus declining,[30] the changes reported here are much more dramatic.

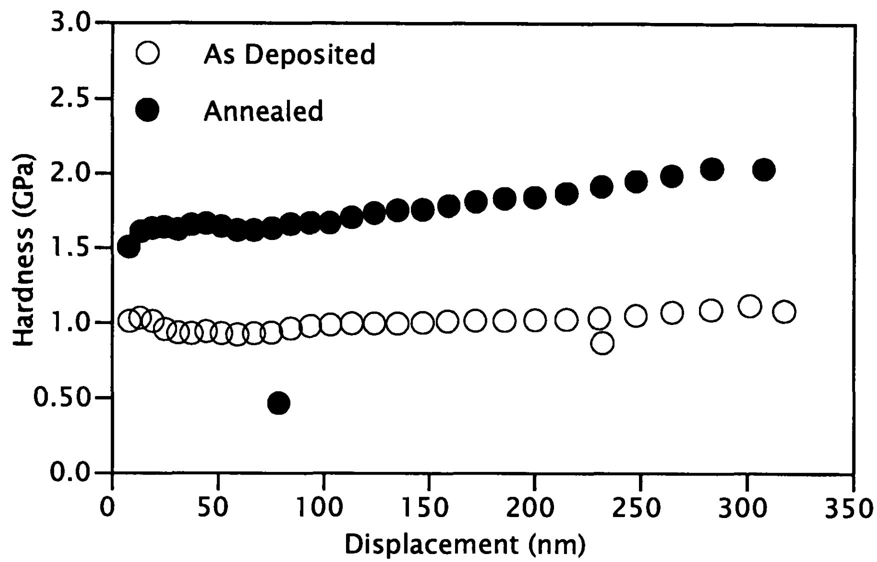

Figure 2-3: Displacement into surface versus hardness plot for as-deposited (open markers) and annealed (solid markers) films, with significant increase seen upon annealing.

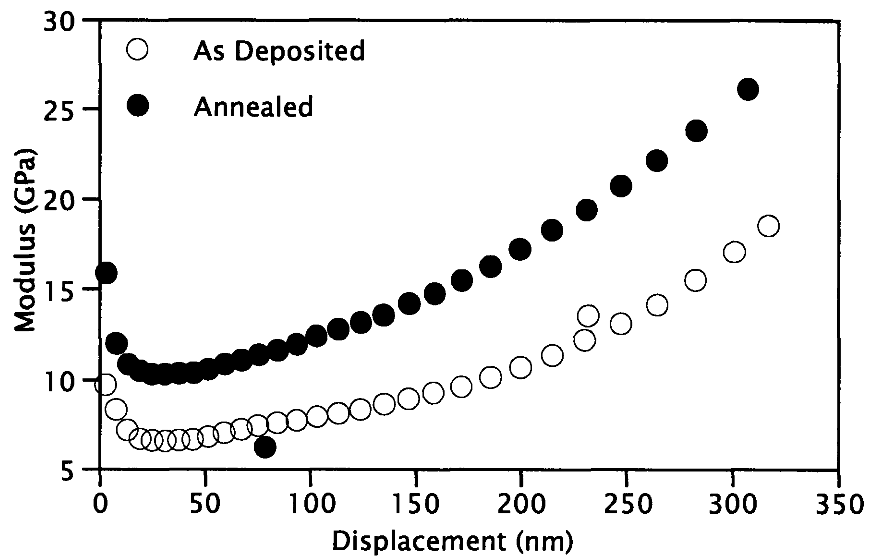

Figure 2-4: Displacement into surface versus elastic modulus plot for as-deposited and annealed films, with significant increase seen upon annealing

2.5 EFFECT OF PROCESSING CONDITIONS

2.5.1 FLOW RATE RATIOS

The effect of varying the O2 to DES flow rate ratio has significant effect on the film properties. The O2:DES ratio was changed from 10:7 to 15:7 to 20:7 while holding all other variables constant. Increasing this ratio caused the deposition rates to increase proportionally, rising from 65.2 to 73.6 to 89.7 nm/min, with standard deviations below 1.5 nm/min. Both hardness and modulus increased significantly with increased oxygen flow rate, as shown in Figure 2-5 and Figure 2-6. The higher percentage of O2 in the gas feed results in greater incorporation of oxygen into the film structure and thereby creates a more cross-linked material. Again, there is a significant jump in the mechanical properties upon annealing due to the condensation reaction that occurs between proximal -OH end groups. A slight decrease in index of refraction can be seen with increased oxygen flow, with values around 1.44. After annealing, the index of refraction drops into the 1.42-1.43 range.

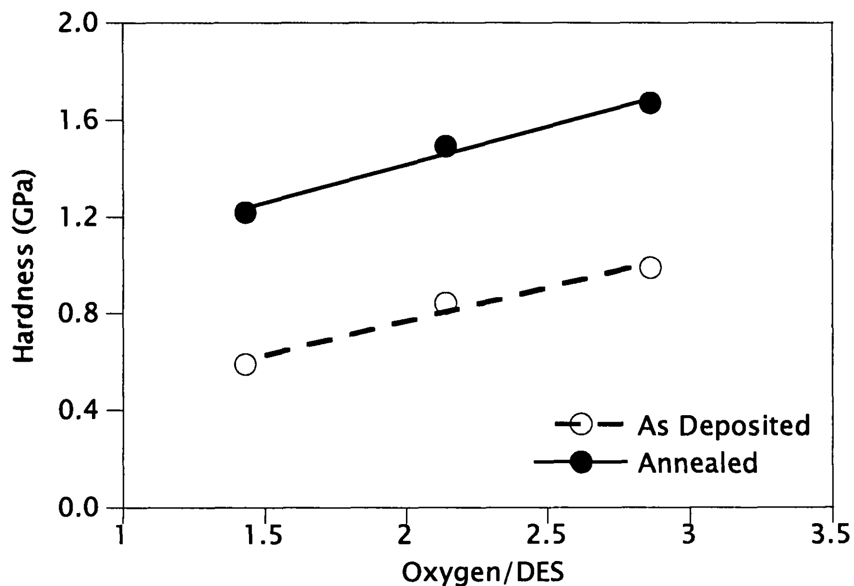

Figure 2-5: Effect of precursor flow rate ratios on hardness.

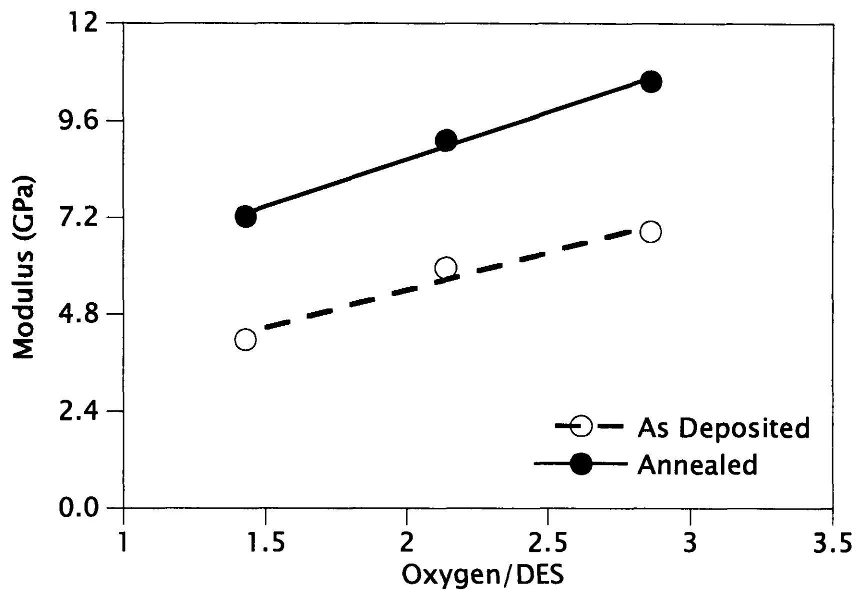

Figure 2-6: Effect of precursor flow rate ratios on elastic modulus.

2.5.2 Plasma Processing Conditions

Pulsed plasma enhanced CVD is a commonly used method to further tune the film properties and is accomplished by turning the plasma off and on in set intervals.[30,34,35] This method of plasma deposition proved less problematic, as it was observed that pulsing reduced particle generation in this work. The pulse rate was changed, while holding the duty cycle (plasma on time / total cycle time) constant at 25%. The peak power remained constant at 200 W, allowing the equivalent power (duty cycle * peak power) to remain fixed at 25 W. The resulting deposition rates and indices of refraction are shown in Figure 2-7. The index of refraction increases with shorter on/off-times (i.e. 10/30) representing an increase in the dielectric constant. However, this also leads to a higher deposition rate.

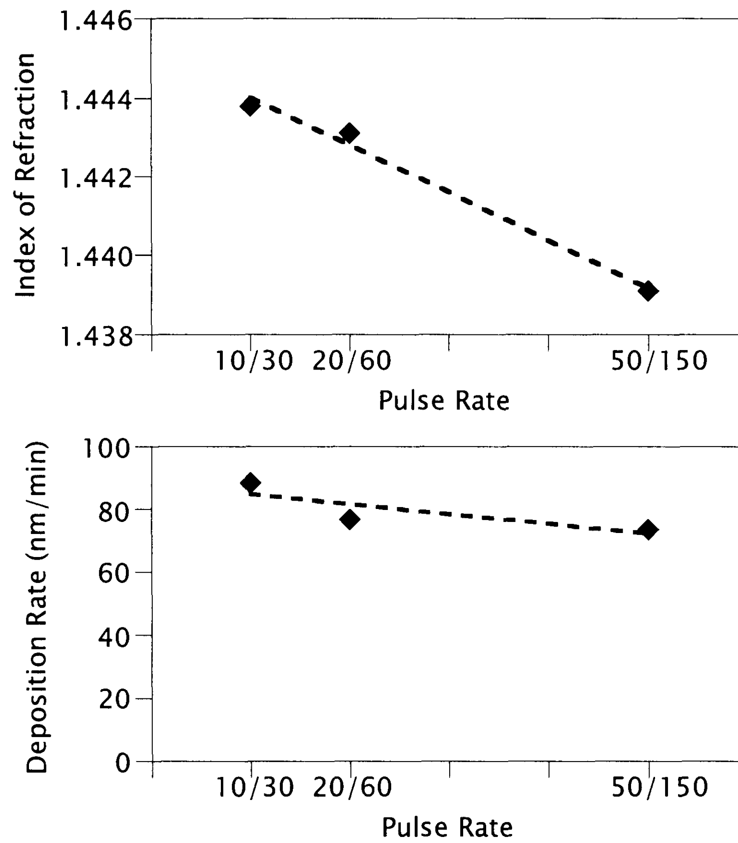

Figure 2-7: Refractive indices and deposition rates versus plasma pulsing conditions.

The duty cycle was also varied while maintaining a constant equivalent power, and the results are shown in Figure 2-8. A higher duty cycle results in higher indices of refraction as well as higher depositions rates.

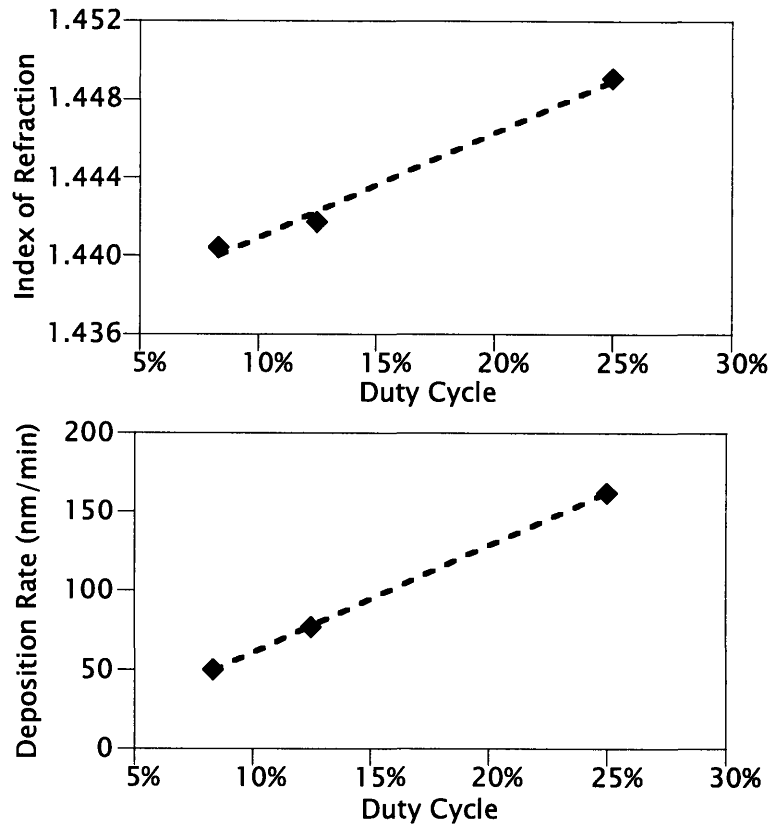

Figure 2-8: Refractive Indices and Deposition rates versus duty cycle

2.6 Conclusions

OSG thin films were deposited using diethylsilane and oxygen via pulsed-PECVD. The FTIR spectrum confirmed significant organic content (CH_2, CH_3) as well as a considerable hydroxyl inclusion from water impurities. Although diethylsilane was the chosen precursor due to the higher organic content that its methyl silane counterparts, the high organic content can ultimately be the limiting factor with DES if carbon bridging occurs and silicon carbide formation begins. Upon annealing at 400 °C, the hydroxyl groups were removed and intensity of the primary Si-O-Si stretch at 1060 cm^{-1} increased, indicating a condensation reaction is occurring between proximal hydroxyl end groups resulting in a more crosslinked

material. The loss of hydroxyl end groups as well as the decrease in density caused by the condensation resulted in a lower index of refraction post annealing. The increased degree of crosslinking also coincided with improved mechanical properties as seen in other works. In some instances, the hardness more than doubled and the modulus increased by over 50% after annealing. All films showed a modulus of 4.0 GPa or greater, indicating mechanical integrity would remain intact for a standard oxide CMP process.[36]

Recently, Burkey's work detailing structural and mechanical properties of OSG materials that employing a similar condensation reaction was reported.[30] Similar structural changes were observed with FTIR however the hardness mostly increased (-6 to 20%) with post-anneal, obtaining a maximum hardness observed 0.527 GPa. However, the increase in modulus detailed in this work was not observed. Indices of refraction ranged from 1.469 to 1.475 for the as-deposited materials and fell to 1.423 to 1.454 for the annealed, a more dramatic decrease than was observed.

Similar OSG materials have been previously produced by CVD using different precursors. Grill and Patel produced low-k materials from tetramethylsilane with indices of refraction ranging from 1.47 to 1.80 and corresponding dielectric constants from 3.0 to 4.5.[37] Pang et al. reported properties for Black Diamond, a silicon dioxide-like material, having a dielectric constant of 2.5 and index of refraction at 1.46.[38]

Changing the relative amounts of oxygen and DES also has a substantial impact on film structure. Increasing the O_2/DES ratio results in greater oxygen incorporation into the film structure, which leads to harder, more crosslinked films. Additionally, both increasing the duty cycle and decreasing the pulse rate results in a denser film with a higher refractive index as well as higher deposition rates. By adjusting these processing parameters, films can be systematically tuned to have

its specific properties; however, there is often a give-and-take between achieving a lower index of refraction and obtaining higher deposition rates.

REFERENCES

1. M. B. Anand, M. Yamada, and H. Shibata, *IEEE Trans. Electron Devices* **44**, 1965 (1997).
2. M. ONeill, A. Lukas, R. Vrtis, J. Vincent, B. Peterson, M. Bitner, and E. Karwacki, *Semiconductor International* (June 2002).
3. D. Thomas, Y. Song, and K. Powell, *Solid State Technol.* **44**, 107 (2001).
4. M. Morgen, E. T. Ryan, C. H. Jie-Jua Hua, T. Cho, and P. S. Ho, *Annu. Rev. of Mater. Sci.* **30**, 645 (2000).
5. A. Grill, *J. Appl. Phys.* **93**, 1785 (2003).
6. E. S. Lopata, L. Young, and J. T. Felts, *Mater. Res. Soc. Symp. Proc.* **612**, D5.3.1 (2000).
7. M. J. Loboda, *Microelectron. Eng.* **50**, 15 (2000).
8. A. Grill and V. Patel, *Appl. Phys. Lett.* **79**, 803 (2001).
9. A. S. Brown, *IEEE Spectrum* **40**, 36 (2003).
10. L. Peters, *Semiconductor International* (May 2002).
11. R. D'Agostino, *Plasma deposition, treatment, and etching of polymers* (Academic Press, Boston, 1990).
12. R. A. Levy, L. Chen, J. M. Grow, and Y. Yu, *Mater. Lett.* **54**, 102 (2002).
13. R. A. Levy, J. M. Grow, and G. S. Chakravarthy, *Chem. Mat.* **5**, 1710 (1993).
14. J. M. Grow, R. A. Levy, Y. T. Shi, and R. L. Pfeffer, *J. Electrochem. Soc.* **140**, 851 (1993).
15. R. A. Levy and J. M. Grow, *Mater. Sci. Eng. B-Solid State Mater. Adv. Technol.* **17**, 172 (1993).
16. J. D. Patterson and M. C. Ozturk, *J. Vac. Sci. Technol. B* **10**, 625 (1992).
17. S. M. George, P. A. Coon, M. L. Wise, A. C. Dillon, and M. B. Robinson, *Abstr. Pap. Am. Chem. Soc.* **202**, 8 (1991).
18. P. A. Coon, M. L. Wise, A. C. Dillon, M. B. Robinson, and S. M. George, *J. Vac. Sci. Technol. B* **10**, 221 (1992).
19. D. T. C. Huo, M. F. Yan, and P. D. Foo, *J. Vac. Sci. Technol. A* **9**, 2602 (1991).
20. K. Usami, S. Sugahara, M. Kobayashi, K. Sumimura, T. Hattori, and M. Matsumura, *J. Non-Cryst. Solids* **260**, 199 (1999).
21. Q. G. Wu and K. K. Gleason, *J. Vac. Sci. Technol. A* **21**, 388 (2003).
22. R. F. Cook, E. G. Liniger, D. P. Klaus, E. E. Simonyi, and S. A. Cohen, *Mater. Res. Soc. Symp. Proc.* **511**, 33 (1998).
23. L. H. Lee, W. C. Chen, and W. C. Liu, *J. Polym. Sci. Pol. Chem.* **40**, 1560 (2002).
24. H. C. Liou and J. Pretzer, *Thin Solid Films* **335**, 186 (1998).
25. A. M. Padovani, L. Rhodes, S. A. B. Allen, and P. A. Kohl, *J. Electrochem. Soc.* **149**, F161 (2002).
26. C. C. Yang and W. C. Chen, *J. Mater. Chem.* **12**, 1138 (2002).

27. H. G. Tomkins and W. A. McGahan, *Spectroscopic Ellipsometry and Reflectometry: A User's Guide* (Wiley-Interscience, New York, 1999).
28. J. H. Mulvey, *The Nature of Matter* (Oxford University Press, New York, 1981).
29. C. J. F. Böttcher, O. C. van Belle, P. Bordewijk, and A. Rip, *Theory of Electric Polarization*, 2nd ed (Elsevier Scientific Pub. Co., New York, 1973).
30. D. D. Burkey and K. K. Gleason, *J. Appl. Phys.* **93**, 5143 (2003).
31. B. C. Bunker, D. R. Tallant, T. J. Headley, G. L. Turner, and R. J. Kirkpatrick, *Phys. Chem. Glasses* **29**, 106 (1988).
32. A. J. Moulson and J. P. Roberts, *Trans. Faraday Soc.* **57**, 1208 (1961).
33. D. H. Levy, K. K. Gleason, M. Rothschild, J. H. C. Sedlacek, and R. Takke, *Appl. Phys. Lett.* **60**, 1667 (1992).
34. H. Yasuda and T. Hsu, *J. Polym. Sci., Polym. Chem. Ed.* **15**, 81 (1977).
35. Y. Wu, L. Han, B. Thomes, H. Qiu, C. Savage, W. Lee, and R. Timmons, *Mater. Res. Soc. Symp. Proc.* **544**, 77 (1999).
36. E. T. Ryan, S. Lin, D. Nelsen, J. T. Wetzel, D. Gidley, and J. Drage, *Advanced Metallization Conference 2001, Proceedings of the Conference* (Pittsburgh, 2001), 557.
37. A. Grill and V. Patel, *J. Appl. Phys.* **85**, 3314 (1999).
38. B. Pang, W. Yau, P. W. Lee, and P. Naik, *Semiconductor Fabtech* **10**, 285 (1999).

CHAPTER THREE

EFFECTS OF CONDENSATION REACTIONS ON THE STRUCTURAL, MECHANICAL, AND ELECTRICAL PROPERTIES OF PLASMA-DEPOSITED ORGANOSILICON THIN FILMS FROM OCTAMETHYLCYCLOTETRASILOXANE

A. D. Ross and K. K. Gleason

ABSTRACT

Organosilicon thin films were deposited from octamethylcyclotetrasiloxane and hydrogen peroxide using pulsed-plasma enhanced chemical vapor deposition. FTIR analysis shows significant organic content as well as hydroxyl and silanol moieties present in the as-deposited materials. Complete removal of the hydroxyl groups after annealing at 400 °C for 1 hour was confirmed by FTIR and indicates that a condensation reaction between proximal hydroxyl groups occurs. This leads to the formation of additional Si-O-Si linkages, also confirmed by FTIR, and these structural changes lead to increased mechanical properties for the film. Mechanical property measurements were in accordance with this hypothesis, as the hardness increased between 46 and 125% after annealing. The structure-hardness relationship was evaluated in the framework of the continuous random network theory and a percolation of rigidity was observed at a connectivity number of 2.35-2.4. Dielectric constant of the annealed films ranged between and 2.78 and 3.20. Film structure and properties were strongly dependent on the feed rate of the oxidant relative to that of the siloxane.

3.1 Introduction

As feature sizes for integrated circuits continue to shrink, the semiconductor industry is focusing technology to minimize the intrinsic time delay for signal propagation, quantified by the RC delay. One avenue for reduction in the RC delay is to lower the capacitance, C, between the wires by decreasing the dielectric constant, *k*.[1] One important class of low-*k* materials is the carbon-doped silicon oxides, also known as organosilicate glasses (OSGs).[2,3] The Si-C bonds in OSGs are more covalent in nature than the Si-O bonds, since Si and O have a large electronegativity difference giving ionic character to their bonds leading to increased polarizability and hence higher dielectric constants.[4] Furthermore, OSG materials have been examined for their ability to create pseudo-porosity by loosening the dense, crosslinked SiO_2 lattice, as a proportion of the Si-O bonds are terminated by methyl groups bound to Si atoms.[5] Additionally, heavier Si and O atoms are replaced with lighter C and H atoms resulting in a reduction in the film density, decreasing the *k*-value.[3,4] Today, dense OSG thin films generally yield dielectric constants ranging from 2.4 to 3.3.[6-9]

Chemical vapor deposition (CVD) is a commonly used deposition technique in semiconductor manufacturing.[10] CVD utilizes gas phase chemistries in a low to ultra-low pressure environment to produce well-defined, high quality films in a controllable and tunable fashion.[11] In this work, OSG thin films were created from octamethylcyclotetrasiloxane (D_4), a cyclic organosilcon, and a hydrogen peroxide solution, which is used as an oxidant . The D_4 precursor has previously been used to produce SiO_2-based thin films using a plasma-enhanced CVD,[12] pyrolytic CVD,[13,14] and pulse-modulated microwave ECR.[15] D_4 is advantageous as it inherently has the built in the desired siloxane (Si-O-Si) linkages along with organic

content ($Si-CH_3$), unlike the silane precursors often used, which lack any Si-O bonds.

The successful integration of OSG films in advance microelectronic devices is dependent on the improvement of their mechanical properties.[16] The addition of organics to the silicon dioxide lattice reduces the network bonding and results in a more open structure with a reduced density. This results in reduced mechanical properties and creates issues with latter processing steps, such as the ability to survive chemical-mechanical polishing.[2,16] Spin-on deposition, another technique sometimes used for low-k materials, relies on a thermal curing step that leads to a structural transformation which supplies the material's strength.[17-21] Often utilizing alcohol or water condensation chemistry, reactions between proximal end groups help to crosslink the film, thereby making it mechanically robust. Burkey recently extended this concept to CVD processes by using a water oxidant during deposition.[22,23] This work further explores the ability of condensation chemistry to improve the mechanical properties of CVD OSG films by using hydrogen peroxide as the oxidant during deposition. Hydrogen Peroxide has several foreseeable advantages over water. First, each molecule can produce two hydroxyl groups while each water molecule can generate only one. Additionally, the H-OH bond in water has a high bond dissociation energy of 118 kcal,[24] while the HO-OH bond in hydrogen peroxide has a much lower dissociation energy of 51 kcal,[25] making it easier to break. Water is also more likely to produce hydrogen radicals which can lead to the formation of Si-H bonds which are undesirable due to their higher polarizability,[26] which leads to higher dielectric constants, as well as their high reactivity which can also cause difficulties during later processing steps.[27]

3.2 EXPERIMENTAL

Depositions were carried out in a custom-built, parallel-plate vacuum chamber described elsewhere.[28] The PECVD system has an upper electrode powered by a 13.56 MHz RF source with attached matching network and a grounded lower electrode. The lower electrode also functions as the substrate stage and was kept at room temperature using a water cooled system. In addition, electrostatic clamping capabilities were utilized to help maintain constant substrate temperatures. The substrates used were 100 mm diameter silicon wafers. The upper electrode / shower-head distributes all incoming precursor gases over the substrate. Octamethylcyclotetrasiloxane (D_4, Gelest Inc., CAS 556-67-2, 98%) was the monomer used with no further purification and hydrogen peroxide (H_2O_2, Sigma Aldrich, 50% aqueous solution, CAS 7722-84-1) was used as an oxidant. Both the D_4 and oxidant were volatilized in a glass jars and delivered to the reactor chamber through a calibrated needle valves. For all depositions, chamber pressure was maintained at approximately 300 mTorr and is controlled by a butterfly valve connected to an MKS model 252A exhaust valve controller. When investigating thermal stability, films were annealed at 400 °C and ambient pressure in a nitrogen atmosphere for one hour.

Fourier Transform Infrared (FTIR) Spectroscopy was performed on a Thermo Nicolet Nexus 870 ESP spectrometer in transmission mode at 4 cm^{-1} resolution using 64 scan averaging. A 10 minute nitrogen purge was performed between each measurement to diminish the effects of carbon dioxide and moisture. All spectra were baseline corrected and had their intensity normalized to a thickness of 5000 Å using their measured thicknesses and Beer's Law.

Film thicknesses and indices of refraction (n_{633}) were determined using VASE, Variable angle spectroscopic ellipsometry, performed on A Woolam M-2000

spectrometer having a xenon light source.. Data was acquired at three angles (65°, 70°, and 75°). The Cauchy model[29] was used to fit the data and the mean-squared errors (MSE) was low (<10), signifying a match between the model and the data.

Electrical measurements to determine dielectric constants were performed using a mercury probe instrument from MDC. A 1 MHz frequency was used and the mercury sport size was nominally 790 μm.

Mechanical properties were measured at the Novellus Research Center in Tualatin, Oregon. Measurements of hardness and elastic modulus were performed using a MTS Systems Nano-Indenter XP and MTS patented continuous stiffness measurement technique. With this technique, each indent gives hardness and elastic modulus as a continuous function of the indenter's displacement into the samples. The surface approach velocity was 5 nm/s and the load versus displacement slop was -81.6 N/m. Experiments were terminated at a depth of approximately 300 nm. A Berkovick diamond tip was used in the measurements. The films were 500 nm or greater in thickness to minimize any substrate effects on the results. Fused silica was tested and used as a control sample.

3.3 FTIR and Structure Analysis

Figure 3-1 shows the FTIR spectra of film deposited from a mixture of D_4 and H_2O_2 solution, at varying oxidant flow rates. The oxidant flow rate is the primary variable in controlling not only the oxygen incorporated into the film's backbone structure, but also the amount of silanol bonding, which is necessary to facilitate the condensation reaction during subsequent annealing step. All depositions were carried out with a flow rate of 1 sccm of D_4 using 10/40 ms on-time/ms off-time pulsed plasma excitation and 300 W peak power. Lower power settings allow more structural retention of the precursor ring and functional

retention of the organic content. Additionally, depositions performed using higher powers or continuous plasma with equivalent average power often encountered powered formation. The assignments of the FTIR bands for OSG materials have been previously reported.[23] The peaks in the 3000 - 2850 cm^{-1} region correspond to $-CH_3$ bonds, revealing the significant presence of hydrocarbon content in the film. The broad peak at 3700-3200 cm^{-1}, highlighted in Figure 3-1b, shows considerable free -OH inclusion in the films, most likely due to incorporation of the hydrogen peroxide oxidant, and increases with increasing oxidant flow rate. Hydroxyl incorporation also appears around 920-830 cm^{-1}, signifying the stretch of the silanol (Si-OH) bond.

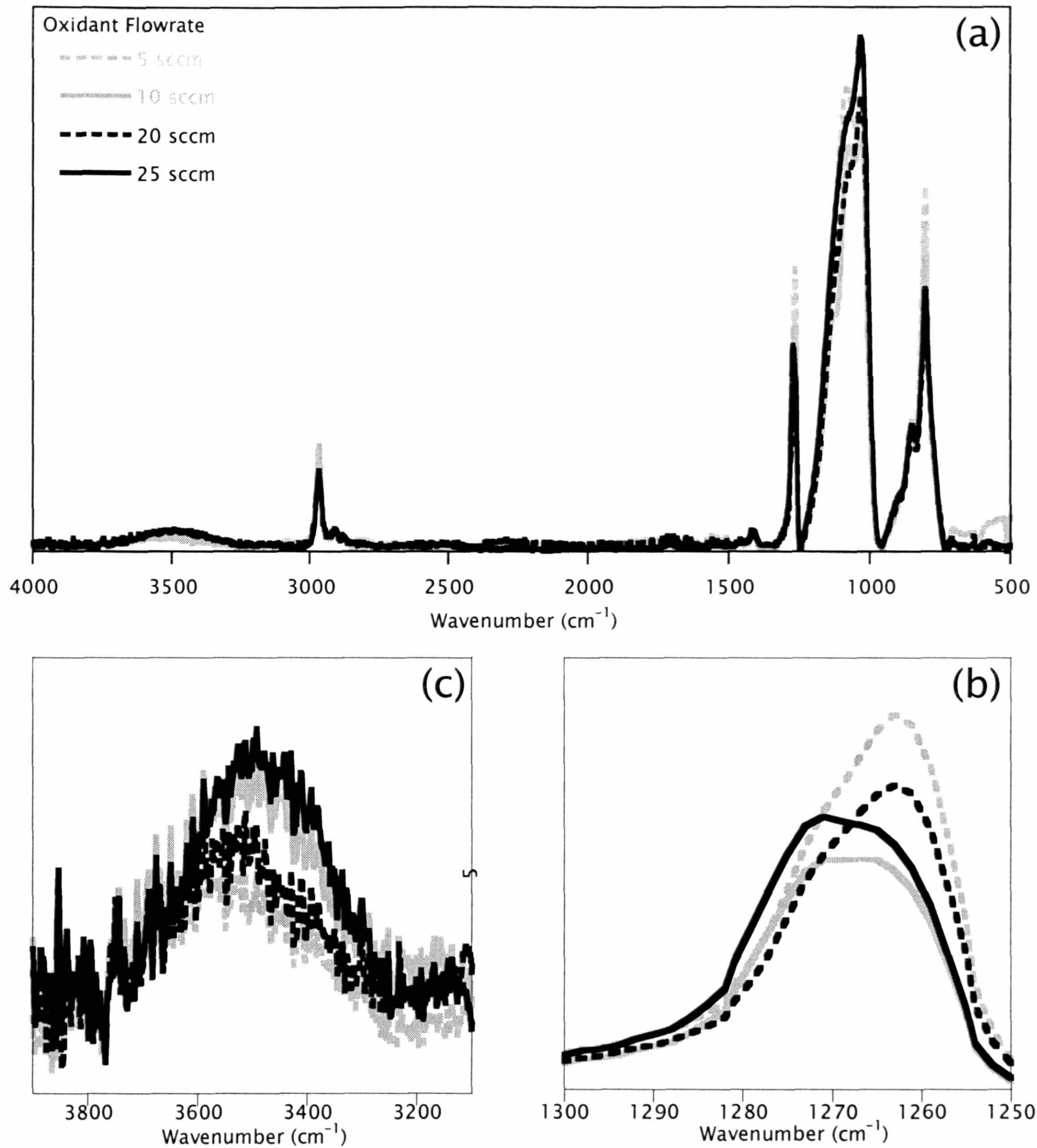

Figure 3-1: FTIR Spectra of films as-deposited at varying oxidant flow rates. (b) expansion of hydroxyl bonding region (c) expansion of Si-$(CH_3)_x$ bonding region.

Also located in this region of the spectrum is Si-C bond, which extends from 870 to 750 cm^{-1} for the Si-CH_3 rock. The Si-O-Si backbone absorbance appears between 1000 and 1200 cm^{-1}, with the rightmost adsorption peak centered around 1020 cm^{-1}. Figure 3-1c magnifies the Si-$(CH_3)_x$ symmetric stretching bands that

occur between 1240-1300cm^{-1}. Further analysis of this area can give a significant insight into the bonding environment of the material. The main building blocks for OSG materials are "M", "D", "T", and "Q" groups, corresponding to mono-, di-, tri -, and quad- oxygen substituted silicon atoms. The first three groups appear at 1250, 1260, and 1270 cm^{-1}, respectively, and spectral curve fitting of this region is used to determine the relative amounts of these groups, which is simply proportional to the area under the peaks. Since Q groups contain no Si-C bonding, they are encompassed in the Si-O-Si peak and the relative intensities cannot be compared. Figure 3-2 shows the ratio of T groups to D groups at varying oxidant flow rates both as-deposited and after annealing; no M groups are apparent in any of the films. As expected, increasing amounts of T groups relative to D groups can be seen with increasing oxidant flow rate, since more oxygen is incorporated into the films during deposition leading to a more crosslinked, or T group rich, material.

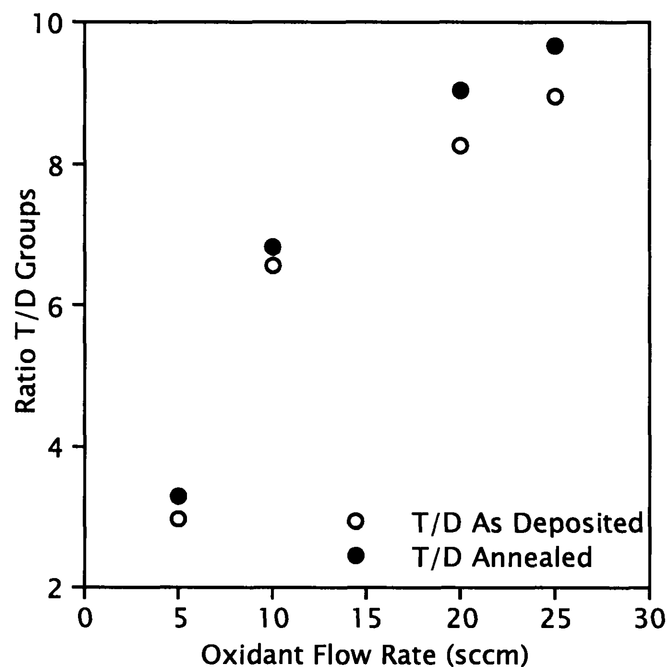

Figure 3-2: Effect of oxidant flow rate on ratio of T groups to D groups, determined by spectral curve fitting.

Figure 3-3 shows the FTIR spectra before and after annealing for the thin film deposition using a 25 sccm oxidant flow rate. Significant changes can be observed in the film structure; most notably, the broad -OH peak highlighted in Figure 3-3b disappears, indicating complete removal of the hydroxyl group after annealing.

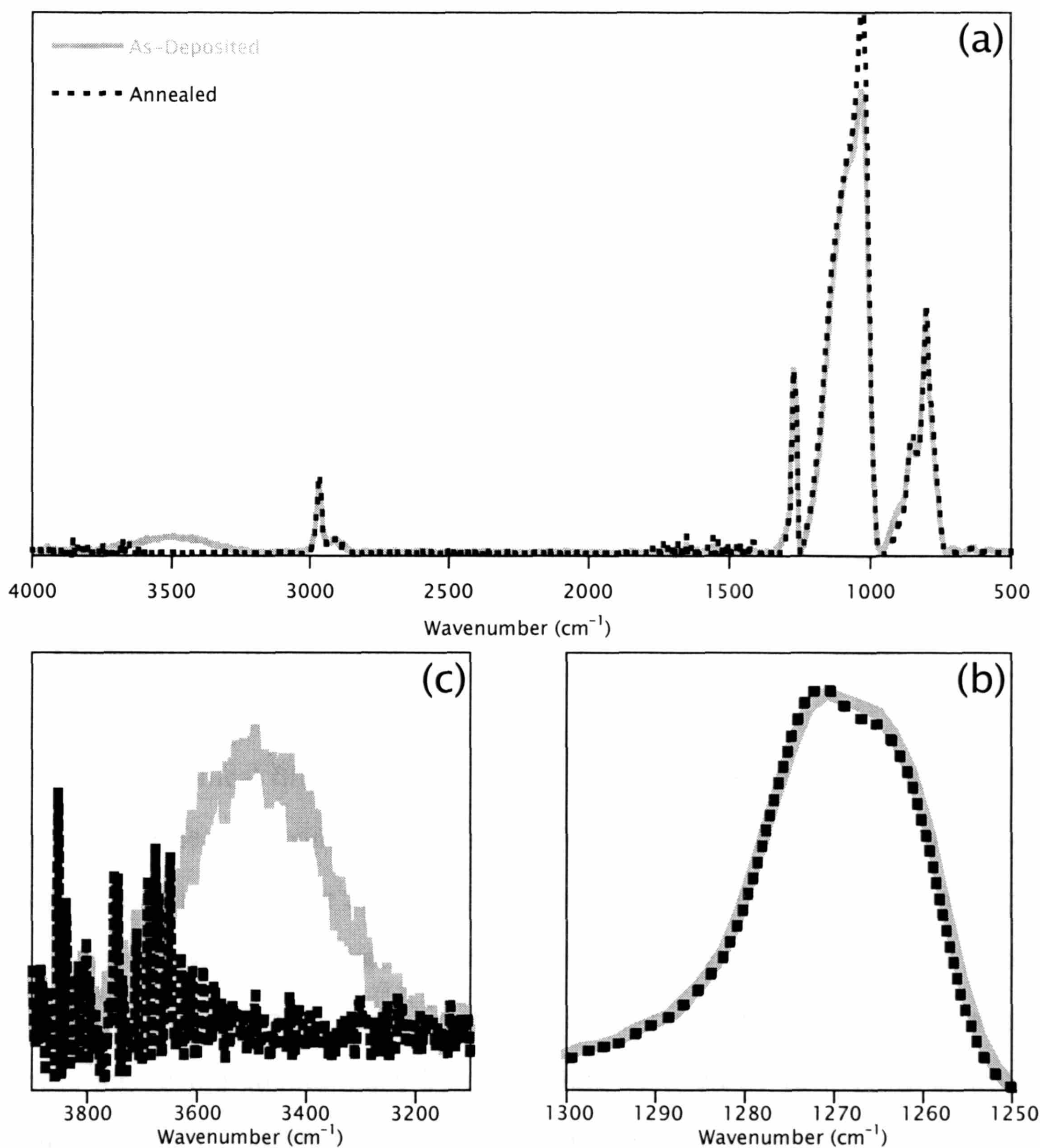

Figure 3-3: FTIR Spectra of a film as-deposited (solid line) and annealed (dashed line). (b) expansion of hydroxyl bonding region (c) expansion of Si-$(CH_3)_x$ bonding region.

Another apparent difference is the increase in intensity of the Si-O-Si peak at 1020 cm^{-1}, indicating the formation of additional Si-O linkages and a shift in the polymer backbone structure. Again, careful examination of the $Si\text{-}(CH_3)_x$ peaks between 1240-1300 cm^{-1} in Figure 3-3c shows a relative increase in T groups after annealing, indicating the formation of additional crosslinks. Figure 3-2 and Figure 3-1 shows the change observed in relative T to D groups after annealing for varying oxidant flow rates. For each deposition, a relative increase in T groups was observed. Combined, these variances can be attributed to adjacent Si-OH groups undergoing a condensation reaction as outlined below.[30-32]

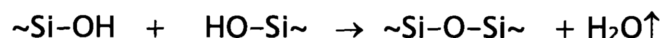

$$\sim Si\text{-}OH + HO\text{-}Si\sim \rightarrow \sim Si\text{-}O\text{-}Si\sim + H_2O\uparrow$$

In this reaction, the additional Si-O networking bonds created lead to a higher crosslinked film and improved mechanical strength.[23] In the absence of film shrinkage, the loss of water also decreases the overall density of the film.

3.4 Mechanical Properties

The mechanical film properties of the films were examined before and after annealing at different oxidant flow rates. Figure 3-4 shows the hardness versus displacement curves for the as-deposited and annealed films deposited using a 25 sccm oxidant flow rate; Figure 3-5 shows modulus versus displacement. For this case, both hardness and modulus had an increase upon annealing, with the hardness increasing substantially by over 100% from 0.201 to 4.17 GPa, while the modulus improved slightly from 3.23 to 3.36 GPa. These results are attributed to the increased crosslinking confirmed by FTIR.

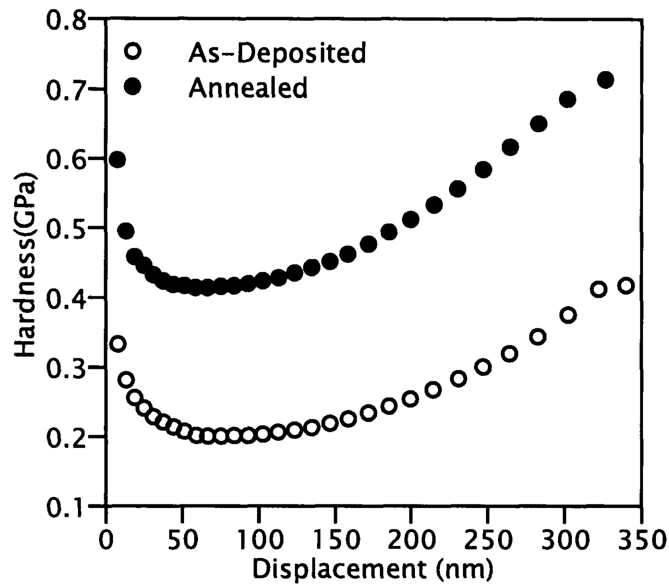

Figure 3-4: Displacement into surface versus hardness plot for as-deposited (open markers) and annealed (solid markers) films, with significant increase seen upon annealing.

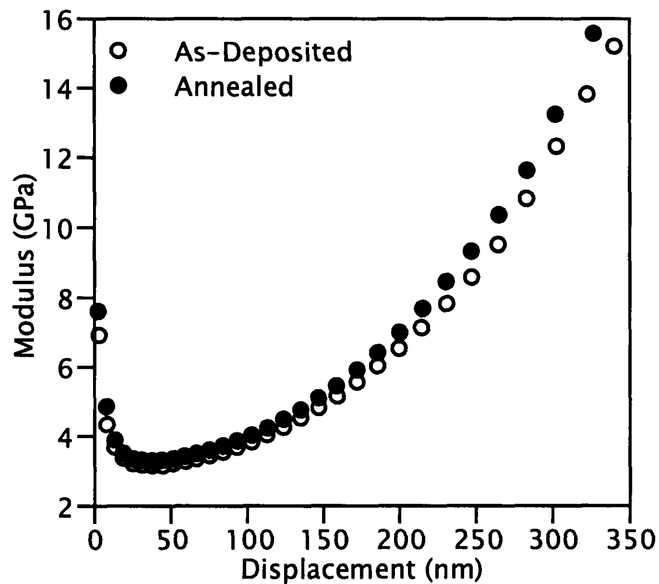

Figure 3-5: Displacement into surface versus elastic modulus plot for as-deposited and annealed films, with increase seen upon annealing.

The effect of varying the oxidant to D_4 flow rate ratio has significant effect on the mechanical properties. Both hardness and modulus increased significantly

with increased oxygen flow rate, as shown in Figure 3-6. The higher percentage of oxidant in the gas feed results in greater incorporation of oxygen into the film structure, thereby creating a more cross-linked material and signifying that higher crosslinking leads to a more rigid, mechanically stable structure. Figure 3-6 also reiterates the trend of improved mechanical properties observed after annealing for all oxidant flow rates. Again, there is a significant jump in the mechanical properties upon annealing due to the condensation reaction that occurs between proximal hydroxyl end groups.

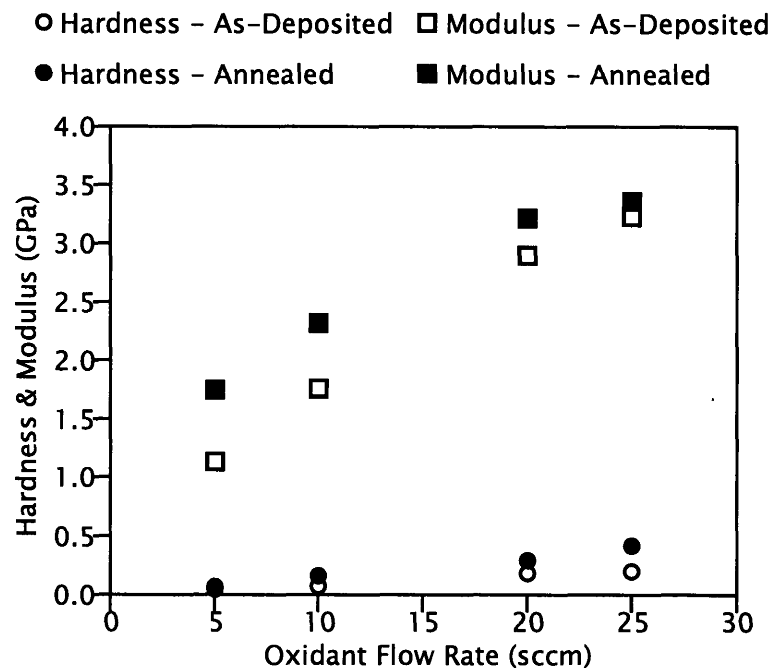

Figure 3-6: Effect of oxidant flow rate on hardness and elastic modulus.

The relationship between the FTIR results and the mechanical properties can be better understood in the context of the continuous random network theory and percolation of rigidity concepts.[33-35] These concepts have previously been discussed in the framework of OSG materials[23] and state that above a certain level of compositional crosslinking, or connectivity, the bonding environment becomes

constrained and experiences improved mechanical properties. The percolation of rigidity occurs as an average connectivity number, which is the number of network forming bonds per networked atom, of 2.4.[34] The connectivity numbers of M, D, and T groups have been previously determined and 1.5, 2.0, and 2.4, respectively.[23] Fully crosslinked SiO_2 is comprised solely of Q groups, which have a connectivity number of 2.67. To calculate these values, the number of network forming bonds in each structural unit was divided that by the number of networked atoms in that unit. Oxygen and silicon atoms are both network forming while carbon is not, since it bonds to only one other network forming atom. For an example, T groups have one silicon atom, which forms 3 networking bonds to oxygen atoms. Each of the three oxygen atoms has two network forming bond for a total of 6; however, since the oxygen atoms are also part of the next structural unit, only half of the bonds are counted. This gives a grand total of 6 network forming bonds. The number of atoms is simply the one silicon plus half of the 3 oxygen atoms, giving a total of 2.5. This leads to the connectivity number of (6/2.5) or 2.4 for each T group.

To determine the average connectivity number of our films, the spectral curve fitting performed on the Si-CH_3 region of the FTIR spectrum used to determine the relative amounts of M, D, and T groups is utilized. However, if the connectivity number calculations were limited to M, D, and T groups, the percolation of rigidity could only be reached with 100% T groups. Therefore, this analysis is taken a step further to include the additional Q groups by comparing the total area of the curves under the Si-CH_3 region of the spectrum. Since all the FTIR spectra were normalized to the same thickness, we can assume approximately the same number of Si atoms are represented in each spectrum. Each silicon atom is bonded to either oxygen or carbon (in the form of methyl groups), indicating that all the silicon exists in the form of M, D, T, or Q groups. Therefore, any differences in the total combined area of the M, D, and T groups between different films can be

attributed to the presence of Q groups. This analysis determines the minimum number of Q groups for each sample, since the film with the largest area is assumed to have no Q groups and is used as the basis for comparison against the other films. Using this approach, the minimum average connectivity number is calculated by simply taking the sum of the weighted contribution of each of the four bonding structures. Table 3-1 summarizes the results of using this calculation method at various deposition conditions.

Table 3-1: Structural composition percentages from FTIR and connectivity numbers

Oxidant Flowrate (sccm)	% D	% T	% Q	Average Connectivity Number
5, As Deposited	25.1	74.9	0.0	2.30
5, Annealed	22.3	73.5	4.2	2.32
10, As Deposited	12.3	80.7	7.0	2.37
10, Annealed	11.3	77.2	11.5	2.39
20, As Deposited	9.1	75.1	15.8	2.41
20, Annealed	7.8	70.2	22.1	2.43
25, As Deposited	9.0	80.2	10.8	2.39
25, Annealed	7.5	72.2	20.4	2.43

Figure 3-7 shows the average connectivity number versus hardness for the same samples. Two trends are clearly visible, with a sharp increase in mechanical strength seen at a connectivity number around 2.35-2.4, indicating the point of the percolation of rigidity.

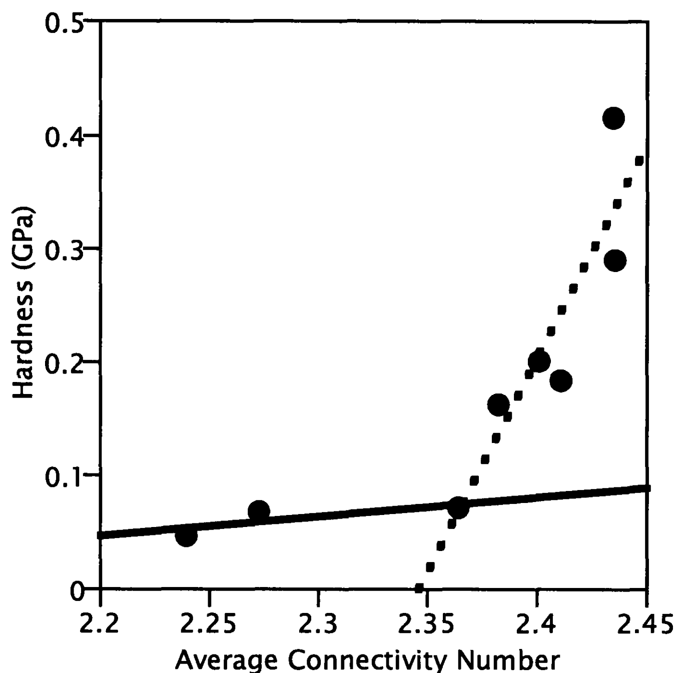

Figure 3-7: Hardness versus connectivity number.

3.5 ELECTRICAL PROPERTEIES

Dielectric measurements from the as-deposited and annealed films are shown in Figure 3-8. The as-deposited values are artificially high due to the hydroxyl incorporation in the films. Increasing oxidant flow rate corresponds to increased dielectric constants, due to both the higher hydroxyl content as well as more initial oxygen incorporation in the backbone structure, which creates a denser material. Annealing the samples and thereby removing the hydroxyl groups drops the dielectric constant down to values typical for OSG materials, ranging from 2.78 to 3.20. These values are significantly lower that that of SiO_2, which has a dielectric constant of 4.2. Literature values for OSG materials created by CVD from ring-structured siloxanes range from 2.4 to 4.0.[22,23,36]

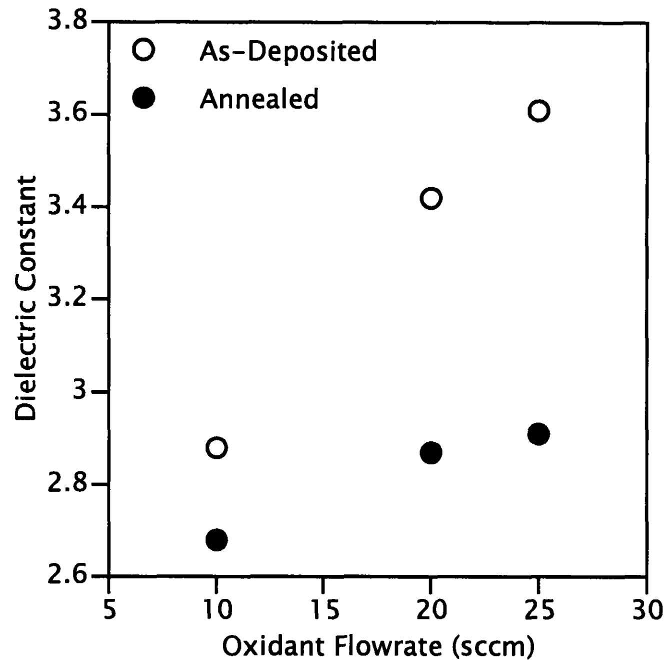

Figure 3-8: Effect of oxidant flow rate and annealing on the dielectric constant.

3.6 CONCLUSIONS

OSG thin films with systematically increasing oxygen content were deposited using octamethylcyclotetrasiloxane with increasing hydrogen peroxide via pulsed-PECVD. Additionally, deposition rates increased with increasing oxidant flow rates, ranging from 81.3 to 104.3 nm/min. Analysis of the FTIR spectra revealed significant amounts of both methyl and hydroxyl groups in the as-deposited films. Subsequent annealing at 400 °C caused a reaction between proximal hydroxyl end groups to form crosslinking bonds, which was verified by close examination of the Si-CH_x stretches in the region between 1240-1300 cm^{-1}, and the relative amounts of M, D, and T groups were determined by spectral curve fitting. This increased degree of crosslinking also coincided with improved mechanical properties. In some instances the hardness more than doubled upon annealing, increasing

anywhere from 46 to 125%, while the modulus increased by more modest amounts, ranging from 4 to 54%. Previous studies on the changes in mechanical properties of OSG thin films as a result of crosslinking induced during anneal reported the hardness increasing between 1-20%, while the modulus declined.[23] Film thickness retention after annealing was >94% demonstrating reasonable thermal stability. Dielectric constants for the annealed films ranged from 2.78 to 3.20; these values were significantly lower than their as-deposited counter part due to the loss of hydroxyl end groups as well as the decrease in density caused by the condensation. Similar OSG materials have been previously produced by CVD using different precursors. Grill and Patel produced low-k materials from tetramethylsilane with dielectric constants from 3.0 to 4.5.[37] Burkey produced OSG thin films for various cyclic siloxane precursors, with dielectric constants ranging from 2.4 to 4.0.[22,23] Widodo reported dielectric constants of 3 to 3.2 from for materials deposited from tetramethylcyclotetrasiloxane.[36]

Changing the oxidant flow rate also has a substantial impact on film structure. Increasing the oxidant flow rate results in greater oxygen incorporation into the film structure, which leads to harder, more crosslinked films. The relationship between the degree of crosslinking in the film structure and the mechanical strength of the materials was explored in the framework of the continuous random network theory. The minimum average connectivity number was calculated and the percolation of rigidity was observed at a connectivity number 2.35-2.4, which corresponds well with literature values.

1. M. B. Anand, M. Yamada, and H. Shibata, *IEEE Trans. Electron Devices* **44**, 1965 (1997).
2. M. ONeill, A. Lukas, R. Vrtis, J. Vincent, B. Peterson, M. Bitner, and E. Karwacki, *Semiconductor International* (June 2002).
3. D. Thomas, Y. Song, and K. Powell, *Solid State Technol.* **44**, 107 (2001).
4. M. Morgen, E. T. Ryan, C. H. Jie-Jua Hua, T. Cho, and P. S. Ho, *Annu. Rev. of Mater. Sci.* **30**, 645 (2000).
5. Y. H. Kim, S. K. Lee, and H. J. Kim, *J. Vac. Sci. Technol. A-Vac. Surf. Films* **18**, 1216 (2000).
6. A. Grill, *J. Appl. Phys.* **93**, 1785 (2003).
7. E. S. Lopata, L. Young, and J. T. Felts, *Mater. Res. Soc. Symp. Proc.* **612**, D5.3.1 (2000).
8. M. J. Loboda, *Microelectron. Eng.* **50**, 15 (2000).
9. A. Grill and V. Patel, *Appl. Phys. Lett.* **79**, 803 (2001).
10. L. Peters, *Semiconductor International* (May 2002).
11. R. D'Agostino, *Plasma deposition, treatment, and etching of polymers* (Academic Press, Boston, 1990).
12. L. Zajickova, J. Janca, and V. Perina, *Thin Solid Films* **338**, 49 (1999).
13. M. C. Kwan and K. K. Gleason, *Chem. Vapor Depos.* **3**, 299 (1997).
14. H. G. P. Lewis, T. B. Casserly, and K. K. Gleason, *J. Electrochem. Soc.* **148**, F212 (2001).
15. Y. Qi and T. D. Mantei, *Surf. Coat. Technol.* **177-178**, 394 (2004).
16. A. S. Brown, *IEEE Spectrum* **40**, 36 (2003).
17. R. F. Cook, E. G. Liniger, D. P. Klaus, E. E. Simonyi, and S. A. Cohen, *Mater. Res. Soc. Symp. Proc.* **511**, 33 (1998).
18. L. H. Lee, W. C. Chen, and W. C. Liu, *J. Polym. Sci. Pol. Chem.* **40**, 1560 (2002).
19. H. C. Liou and J. Pretzer, *Thin Solid Films* **335**, 186 (1998).
20. A. M. Padovani, L. Rhodes, S. A. B. Allen, and P. A. Kohl, *J. Electrochem. Soc.* **149**, F161 (2002).
21. C. C. Yang and W. C. Chen, *J. Mater. Chem.* **12**, 1138 (2002).
22. D. D. Burkey and K. K. Gleason, *J. Electrochem. Soc.* **151**, F105 (2004).
23. D. D. Burkey and K. K. Gleason, *J. Appl. Phys.* **93**, 5143 (2003).
24. L. V. Gurvich, I. V. Veyts, and C. B. Alcock, *Thermodynamic Properties of Individual Substances* (Hemisphere, New York, 1989).
25. W. G. Alcock and E. Whittle, *Trans. Faraday Soc.* **64**, 244 (1965).
26. D. F. Shriver, P. Atkins, and C. H. Langford, *Inorganic Chemistry*, 2nd ed (W. H. Freeman and Company, New York, 1994).
27. S. J. Clarson and J. A. Semlyen, *Siloxane polymers* (PTR Prentice Hall, Englewoods Cliffs, NJ, 1993).

28. H. G. P. Lewis, D. J. Edell, and K. K. Gleason, *Chem. Mat.* **12**, 3488 (2000).
29. H. G. Tomkins and W. A. McGahan, *Spectroscopic Ellipsometry and Reflectometry: A User's Guide* (Wiley-Interscience, New York, 1999).
30. B. C. Bunker, D. R. Tallant, T. J. Headley, G. L. Turner, and R. J. Kirkpatrick, *Phys. Chem. Glasses* **29**, 106 (1988).
31. A. J. Moulson and J. P. Roberts, *Trans. Faraday Soc.* **57**, 1208 (1961).
32. D. H. Levy, K. K. Gleason, M. Rothschild, J. H. C. Sedlacek, and R. Takke, *Appl. Phys. Lett.* **60**, 1667 (1992).
33. J. C. Phillips, *J. Non-Cryst. Solids* **34**, 153 (1979).
34. G. H. Dohler, R. Dandoloff, and H. Bilz, *J. Non-Cryst. Solids* **42**, 87 (1980).
35. M. F. Thorpe, *J. Non-Cryst. Solids* **57**, 355 (1983).
36. J. Widodo, W. Lu, S. G. Mhaisalkar, L. C. Hsia, P. Y. Tan, L. Shen, and K. Y. Zeng, *Thin Solid Films* **462-63**, 213 (2004).
37. A. Grill and V. Patel, *J. Appl. Phys.* **85**, 3314 (1999).

CHAPTER FOUR

NANOPOROUS ORGANOSILICATE GLASS FILMS VIA CHEMICAL VAPOR DEPOSITION ONTO COLLOIDAL CRYSTAL TEMPLATES

Q. Wu, A. D. Ross, and K. K. Gleason

ABSTRACT

Templated nanoporous organosilicate glass (OSG) films with extremely low values of dielectric constant, 1.4, and refractive index, 1.067 were fabricated via chemical vapor deposition. Well-ordered assemblies of polymer nanospheres serve as templates for the pores. To enable three-dimensional crystal templates to form on substrate areas larger than 10 cm^2, a method using rapid evaporation-induced self-assembly of polystyrene (PS) nanospheres was developed. Conformal plasma-enhanced CVD using dimethylsilane and oxygen precursors fills the interstices of the colloidal crystal to form the OSG matrix. With subsequent annealing at 500 °C the labile polymer beads decompose, resulting in a nanoporous organosilicate thin film.

4.1 INTRODUCTION

Porous nanostructured materials have many important uses in a broad range of fields including photonics,[1-4] catalysis,[5-7] and microelectronics.[8-10] In the semiconductor industry, decreasing feature size demands ultra low-k interlayer dielectric materials in order to minimize transmission delays.[8] Reduction in the dielectric constant can be achieved through the addition of pores. Porous materials with dielectric constants in the ultra low-k region (2.5-1.5) have been reported.[9-12] Presently, chemical vapor deposition (CVD) of organosilicate glass (OSG, Si:O:C:H) is one of the standard manufacturing methods for fabricating interlayer dielectrics.

Creating a composite of an OSG matrix with a sacrificial polymer, which is subsequently removed by curing, is one strategy to create pores in OSG materials. The strategy has been extensively applied to OSG film applied by spin-on deposition (SOD)[13-15] and less frequently to CVD OSG film.[16-18] Control over pore size is a critical issue.[19] In particular, it is necessary to avoid "killer pores," having diameters larger than the feature size of the integrated circuit (<100 nm). Using nanoscale preformed polymeric beads to template the pores is one means of controlling pore size and avoiding large pores.

Using polymeric beads as porogens may have additional benefits. Beads which are monodisperse in size can self-assemble and be used to template regular spaced pores, as has been demonstrated in spin-on OSG films.[20] The ordering of the polymeric beads into colloidal crystals has been achieved by several methods, and the crystallization can yield either two or three dimensional crystals of polymeric beads.[21-23] One method flowed solvent through micromachined channels resulting in dense colloidal multilayer arrays.[22] However, this process is slow, requiring about 24 hours, and covers areas of up to only 1 cm^2. Vlasov et al. reported a temperature gradient method[2] in which a silicon wafer was placed

vertically in a vial containing an ethanolic suspension of silica spheres. After assembling spheres of opal onto a substrate, the interstices were filled using low-pressure chemical vapor deposition of polysilicon at elevated temperature, followed by removal of opal via HF etching.[2] In this work, spheres of a thermally labile polymer are assembled via evaporation-induced self-assembly and polymer decomposition is accomplished simply by pyrolysis, eliminating the need for a wet etchant.

Pulsed plasma-enhanced CVD is used to fill the interstitial voids with OSG. Since the crystal template and matrix material are independently generated with this method, the OSG matrix deposition can be optimized separately. The ability to vary the composition of the CVD matrix material without affecting the porogen broadens the scope of envisioned microelectronics and microphotonics applications. Fully dense CVD OSG films with a composition of $Si_wC_xO_yH_z$ have low dielectric constants, in the range of 2.5-2.7.[24]

The ability of the matrix precursors to infiltrate the colloidal crystal is a key factor for the successful fabrication of porous thin films and CVD is an established method recognized for its ability to produce conformal coatings with excellent gap fill.[25,26] Conformal growth, or step coverage, is guided by two mechanisms, the sticking coefficient and the surface diffusion, or mobility.[26,27] The sticking coefficient is the ratio of the rate of precursor species adsorption to the rate at which the precursor species strikes the surface, and is determined by the diffusion of precursor species within the topographical features.[27] In addition to surface coverage and the structure of the precursor species, the sticking coefficient is a strong function of substrate temperature, and decreases with increasing temperature.[28] Surface diffusion is the mobility of the absorbed precursor on the substrate surface and is quantified by the surface residence time.

Improved step coverage has been reported with decreasing deposition rates.[26,27] This suggests that superior gap fill occurs when low concentrations of reactive species are on the substrate surface. This situation is favored by both high substrate temperature and low species concentration in the gas phase. At high substrate temperatures and low growth rates, surface diffusion is fast relative to incoming flex, which allow the absorbed species to diffuse throughout the structure topography.[25-27]

4.2 EXPERIMENTAL

4.2.1 FORMATION OF TEMPLATES

Two grades of polystyrene nanospheres (Interfacial Dynamics) were used fabricate the crystal colloidal templates. One grade had a mean diameter of 96 nm with a standard deviation of 9 nm (9.4 %). The second had a mean diameter of only 15 nm, with a standard deviation of 3 nm (20 %). To create the templates, aqueous suspensions of the polymeric beads), ranging in concentration from 0.1 to 0.5 g/100ml, were distributed over the surface of a silicon wafer, and opposing ends of the substrate were heated to 60-70 °C, as illustrated in Figure 4-1.

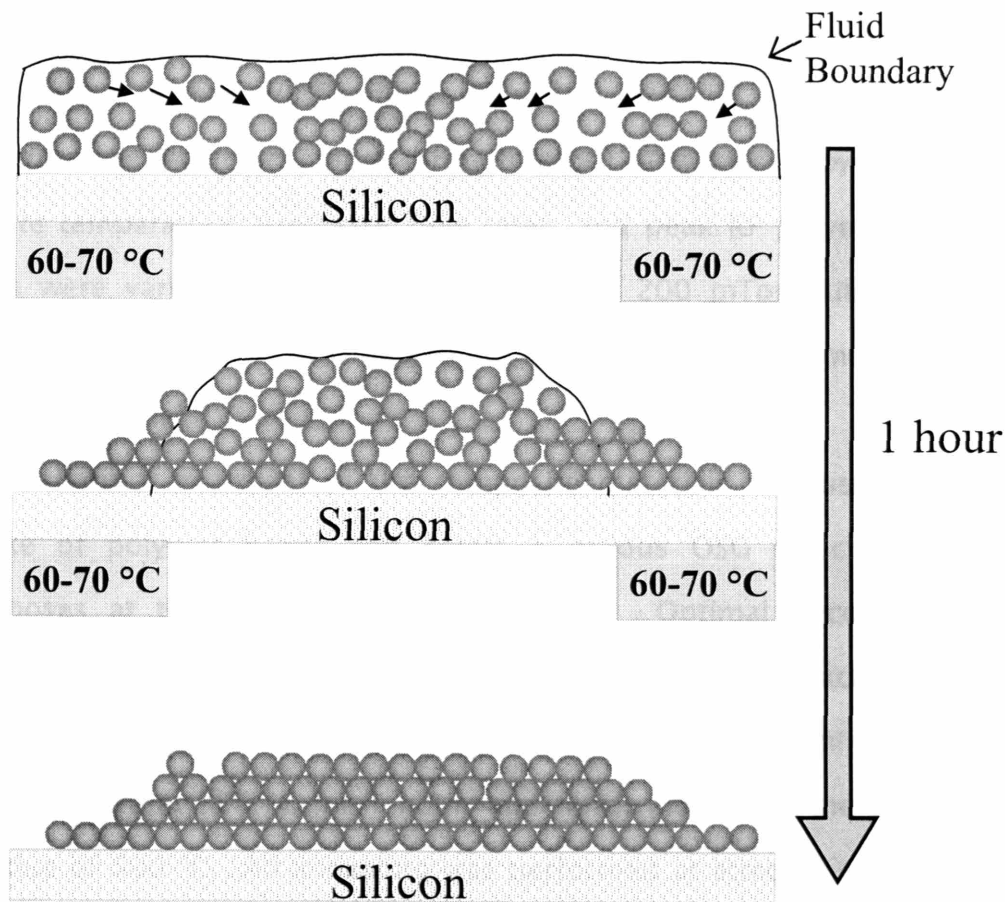

Figure 4-1: Schematic of self-assembly of a colloidal crystal template.

The suspension crystallizes first at the heated edges, propagating the solution toward the cooler center and leading to an ordered, packed array of nanospheres. Arrays as large as 10 cm^2 containing multiple layers of polymer beads were obtained in less than 60 minutes. Varying the concentration of the polymer microspheres in the suspension provides precise control over the number of layers formed, from two to over fifteen.

4.2.2 Pulsed-Plasma Enhanced Chemical Vapor Deposition

Depositions of the organosilicate glass (OSG) were carried out in a custom-built, parallel-plate vacuum chamber, discussed in detail in previous work.[29]

Dimethylsilane (2MS, Voltaix Inc., CAS 0001111-74-6, > 99.98%) was the monomer used with no further purification. The 2MS, oxygen, and argon gases were delivered to the reactor chamber through MKS 1479A Mass Flow Controllers. The substrate temperature, precursor flow rates, and peak RF power of the CVD OSG process were varied 25 °C to 100 °C, 110 to 200 mTorr and 120 to 200 W, respectively. The OSG was deposited on the colloidal templates, creating a composite material.

A thermal treatment of the composite materials was used to remove the template of polymer beads and create a porous OSG structure. Polystyrene decomposes at temperatures above 280 °C.[30] Optimal decomposition occurs without disrupting the surrounding matrix material and was achieved in 3 steps: first, increasing the temperature to 300 °C at a rate of 8 °C/min; second, holding the temperature at 300 °C for 1 hour; and third, increasing the temperature to a final value of 500 °C. All annealing was performed at atmospheric conditions and with a nitrogen purge.

4.2.3 Characterization Methods

Fourier Transform Infrared (FTIR) Spectroscopy was performed on a Thermo Nicolet Nexus 870 ESP spectrometer in transmission mode at 4 cm^{-1} resolution using 64 scan averaging. A 10 minute nitrogen purge was performed between each measurement to diminish the effects of carbon dioxide and moisture. All spectra were baseline corrected and had their intensity normalized to a thickness of 5000 Å using their measured thicknesses and Beer's Law.

Film thicknesses and indices of refraction (n_{633}) were determined using VASE, variable angle spectroscopic ellipsometry, performed on A Woolam M-2000 spectrometer having a xenon light source. Data was acquired at three angles (65°,

70°, and 75°). The Cauchy model[31] was used to fit the data and the mean-squared errors (MSE) was low (<15), signifying a match between the model and the data.

Scanning electron micrograph (SEM) and transmission electron micrograph TEM were performed on a JEOL 6320FV and a JEOL 200CX, respectively

Electrical measurements to determine dielectric constants were performed using a mercury probe instrument from MDC. A 1 MHz frequency was used and the mercury spot size was nominally 790 μm.

4.3 Results and Discussion

SEM and VASE were used to examine the polystyrene nanosphere template created with this method. Figure 4-2 shows the three-dimensional crystal structure of monodispersed, 96 nm diameter beads. The top down view (Figure 4-2a) reveals well-ordered hexagonal arrays of the polymer beads and the cross sectional view (Figure 4-2b) shows five ordered layers of beads. The thickness and refractive index measured were 424.4 nm and 1.3740, respectively. The refractive index is lower than that of pure polystyrene, 1.589 at 20 °C,[32] due to the interstitial air cavities, which have a index of approximately 1.

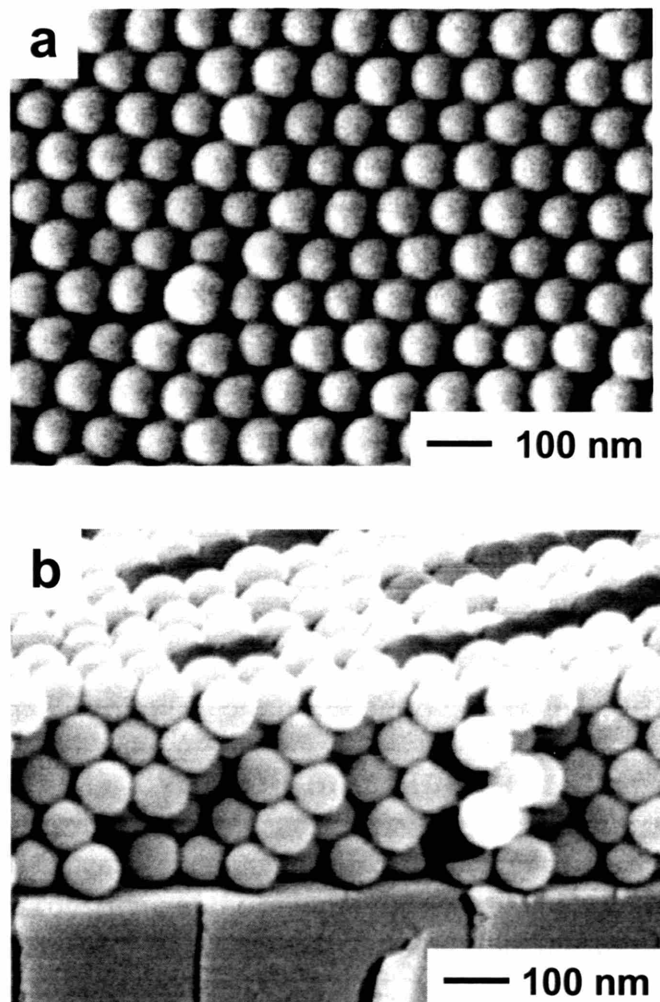

Figure 4-2: SEM images of a five-layer polystyrene template assembled on Si wafer from 96 nm polystyrene nanospheres : (a) Top view; (b) Oblique view.

The OSG material was deposited onto the nanosphere templates to create a composite material. Figure 4-3 shows the FTIR spectra of (a) the polystyrene crystal template, (b) the composite material after deposition of the OSG matrix and (c) the nanoporous OSG film created after thermal treatment.

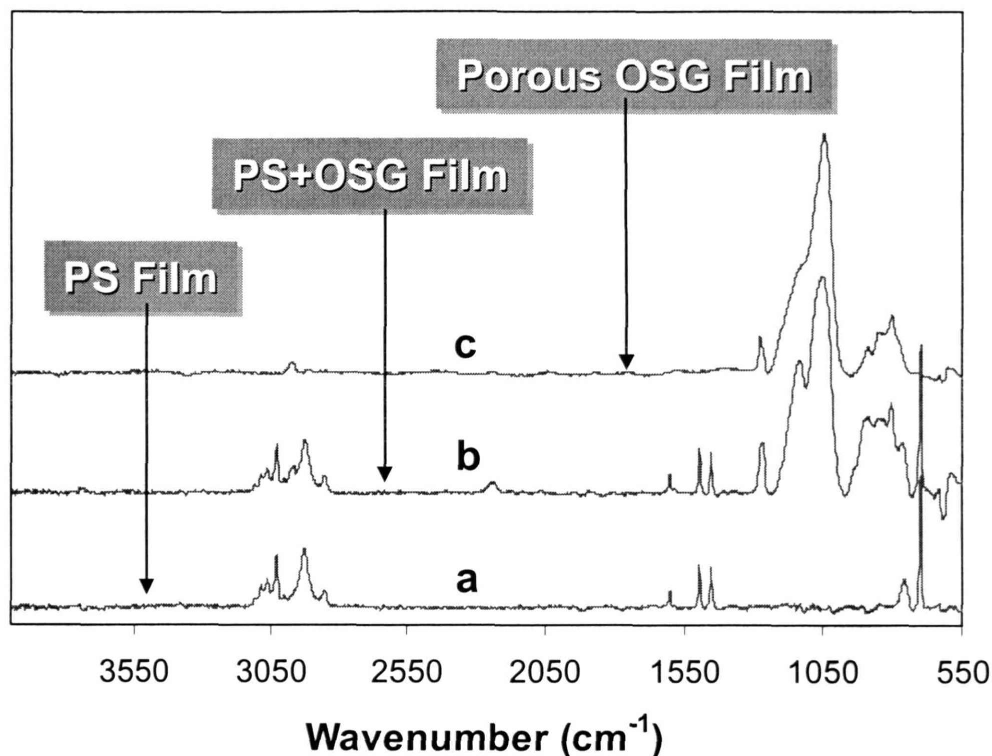

Figure 4-3: FTIR spectra of (a) the template polystyrene nanospheres; (b) the composite film consisting of the template of polystyrene nanospheres filled with CVD OSG and (c) porous OSG film resulting from the decomposition of the polymer beads upon annealing.

The two regions exclusively associated with the polystyrene material are at 700 cm^{-1}, where the phenyl ring deformation occurs, and at 1450-1600 cm^{-1}, where the in-plane C-H stretches appear. These peaks are present in polystyrene and composite films, but are absent in the porous film demonstrating the complete removal of the polystyrene upon annealing. Additionally the $C-H_x$ stretch region associated with the polystyrene appears from 2844-3091 cm^{-1} and the CH_3 stretching bands from OSG is centered at 2960 cm^{-1}. After annealing (Figure 4-3c), only the 2960 cm^{-1} band remains, demonstrating not only the removal of the polystyrene but also the retention of the OSG structure.

The OSG matrix material deposition must fulfill several criteria in order to successfully create a porous material. The OSG must be mechanically robust, to avoid collapse when the polystyrene material is removed, and should be chemically stable. Most importantly, the CVD process must exhibit excellent gap fill in order to fill the void volume within multiple layers of polystyrene beads.

As the OSG deposition rate decreased, the degree of gap infiltration was improved. As expected, increasing the substrate temperature, which both decreases the sticking coefficient and improves the surface mobility of adsorbed species, as well as decreasing the reactor pressure, which reduces the rate at which reactive species strike the substrate surface, lowered the deposition rate and improved gap infiltration. A lower sticking coefficient and higher mobility of growth species on the surface allows better permeation of the into the bottom layers of the template.

The degree to which the OSG matrix infiltrated the void volume within the template beads was examined using AFM and VASE. Figure 4-4 shows the surface topography for the unannealed composite film using 96 nm diameter nanospheres at two different OSG deposition rates of 45.8 and 72.0 nm/min.

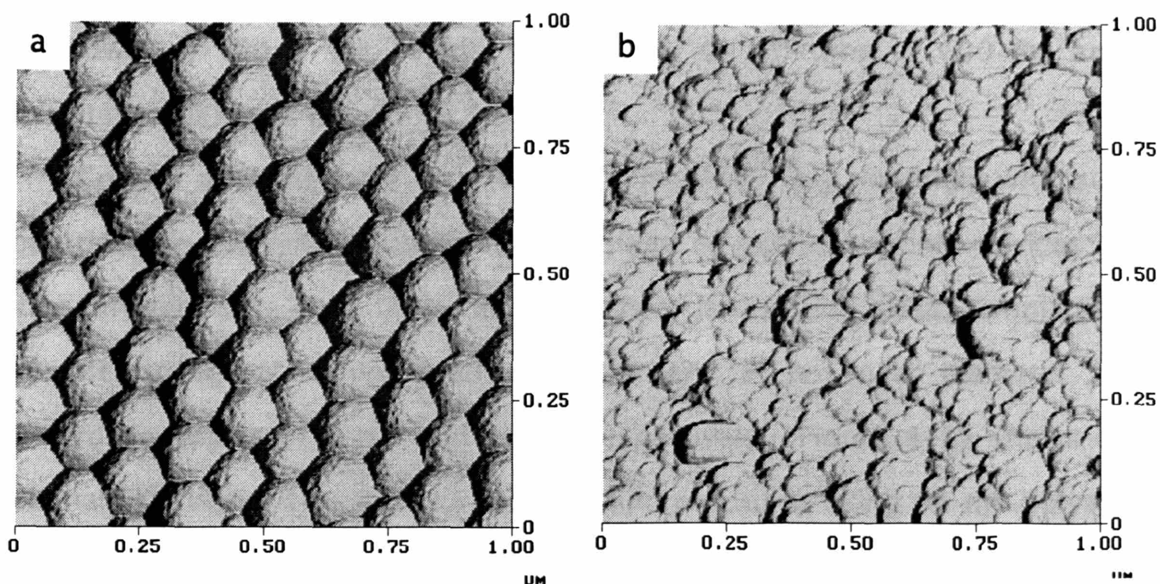

Figure 4-4: AFM of composite materials with OSG deposition rates of (a) 45.8 nm/min and (b)72.0 nm/min.

The slower deposition resulted in a conformal coating while the faster deposition blankets the surface of the template, thereby sealing the gaps on the top bead layer. Examining the refractive indices of these films after annealing gives a further insight into the level of interstitial fill. For a composite material where the OSG has been deposited throughout the entire crystal lattice, as with the slower OSG deposition rate, the matrix structure is able to retain its shape upon removal of the polystyrene to create a porous structure with a low index of refraction of 1.0657. However, when starting with an identical nanosphere template but depositing the OSG at a higher rate of 72.0 nm/min, the gas precursors are unable to permeate throughout the entire polystyrene template before depositing. The matrix material is deposited only in the upper layers of the template and voids spaces are left near the substrate surface. The bottom layers collapsed upon annealing creating a much denser material with an index of refraction of 1.3269. Complete infiltration was achieved using 4 sccm of 2MS, 15 sccm of argon and 2.5 sccm of oxygen at a total pressure of 110 mTorr. The plasma was pulsed with a

peak power of 120 W for 10 ms, followed by an off time of 600 ms and the substrate temperature was 95 °C.

Control over the pore size is critical for obtaining materials with suitable properties for different insulator feature sizes in microelectronic devices.[33] To obtain different pore sizes in the nanoporous organosilicate glass, templates were assembled using polystyrene beads of 96 nm and 15 nm mean diameter, having standard deviations of 9 nm and 3 nm, respectively. Figure 4-5a shows cross-sectional SEM image of a nanoporous OSG film produced using 96 nm polystyrene beads while Figure 4-5b shows TEM image of a film produced using 15 nm polystyrene beads. The ordered pores created by the decomposition of the 96 nm beads are clearly visible while the pores created by the 15 nm beads show greater variability in size due to high standard deviation as a percentage of the mean diameter (20% for the 15nm beads, 9.4% for 96 nm beads) The spherical shape of the voids indicates that the surrounding OSG matrix had sufficient mechanical strength to maintain its structure.

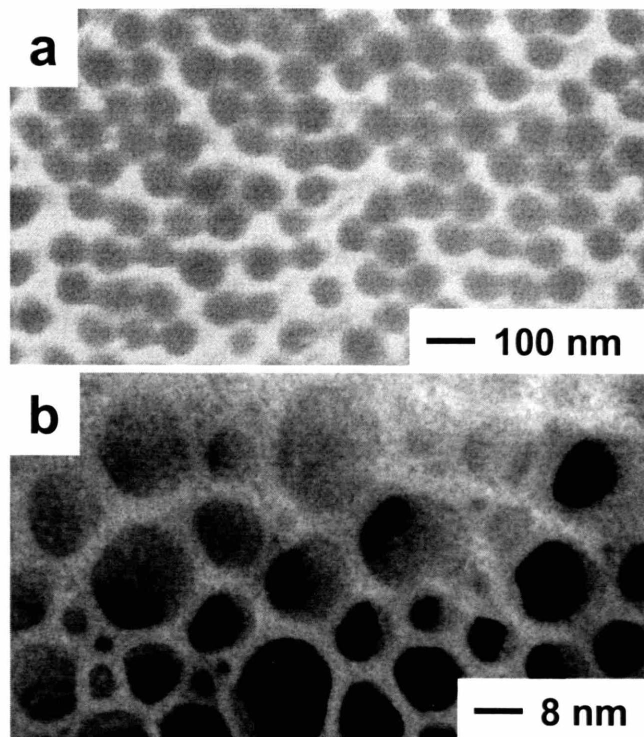

Figure 4-5: Images of porous structures (a) SEM images of nanoporous OSG using 96nm bead template (b) TEM image of nanoporous OSG film using the 15nm bead template.

To demonstrate the effect of varying template fraction, three films were prepared, all using 2-layer templates of 96 nm beads and identical deposition conditions for the OSG matrix. Only the thickness of the OSG deposited was changed, in order to vary the relative amounts of porogen and matrix materials. For the thinnest composite film, the composite thickness was essentially the same as the 2-layer template, leading to a very high template fraction. Longer depositions resulted in different thickness overcoats of dense OSG material on top of the composite layers. The percentage of template in each of the three composite films was calculated assuming hexagonal packing of the 96 nm beads into a 2-layer structure and the measured thickness of the composite film.

Figure 4-6a shows the refractive index as a function of the template percentage for the three composite films. The index of refraction for the dense OSG material, shown where the template percentage is zero, is around 1.4. A linear increase in refractive index with template percentage in the composite films corresponds with the higher fraction of polystyrene, since it has a higher refractive index than the OSG. Also shown in Figure 4-6 are the refractive indices for the annealed samples. Similarly, the linear decrease in refractive index with template percentage corresponds in increasing percentage of porosity. Extending the linear correlation to 100 % gives the expected value of 1, within experimental error.

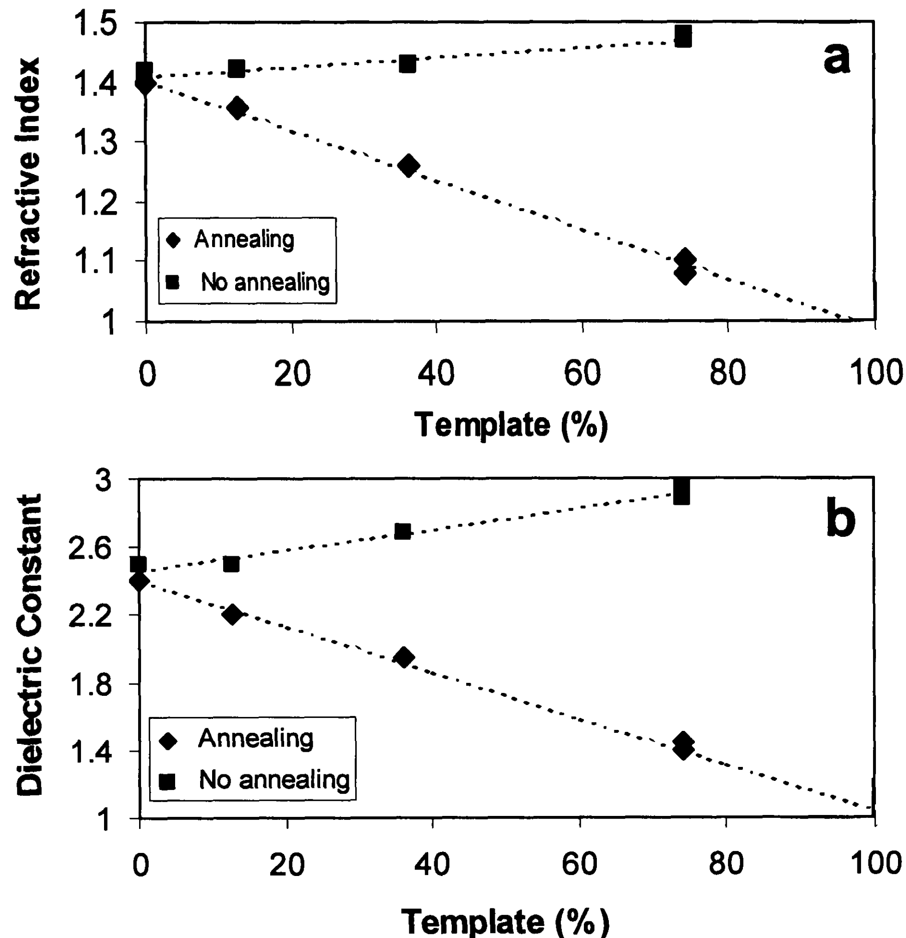

Figure 4-6: Plots of (a) the refractive index versus template percentage and (b) the dielectric constant versus template percentage.

Figure 4-6b shows the dielectric constants at for the same set of films and similar trends can be identified. The dielectric constant of the composite films increases with increasing template percentage, due to polystyrene's higher dielectric constant. The decrease in dielectric constant with template percentage for the annealed films is again attributed to the formation of voids in the film, which contribute a dielectric constant of approximately 1. The highest percent porosity achieved was 74%, and this film produced extremely low values for the refractive index, 1.067, and the dielectric constant, 1.4. Within experimental error, least squares regression of the data extrapolates to the expected value of 1.0 at 100% porosity.

4.4 Conclusions

Nanoporous organosilicate produced by CVD of OSG onto a colloidal template is a new approach to the synthesis of porous thin films, yielding porosities as high as 74% and dielectric constants as low as 1.4. The nanosphere template fabrication using evaporation-induced self-assembly is remarkable for simplicity, speed, and effectiveness in producing large area crystalline templates of well-defined thickness. In addition, the technological steps of CVD and thermal annealing are standard manufacturing techniques. Control over the template area for polymer bead assembly and control over bead shape and size are key issues remaining for the development of this material for practical application. However, this approach may provide an efficient and inexpensive route to integrated circuits for new generation microelectronic devices. Additionally, the low refractive index values and the regularity of the pore structure are attractive for photonic applications.

REFERENCES

1. O. Painter, R. K. Lee, A. Scherer, A. Yariv, J. D. O'Brien, P. D. Dapkus, and I. Kim, *Science* **284**, 1819 (1999).
2. Y. A. Vlasov, X. Z. Bo, J. C. Sturm, and D. J. Norris, *Nature* **414**, 289 (2001).
3. E. Chow, S. Y. Lin, S. G. Johnson, P. R. Villeneuve, J. D. Joannopoulos, J. R. Wendt, G. A. Vawter, W. Zubrzycki, H. Hou, and A. Alleman, *Nature* **407**, 983 (2000).
4. M. Campbell, D. N. Sharp, M. T. Harrison, R. G. Denning, and A. J. Turberfield, *Nature* **404**, 53 (2000).
5. T. Sun and J. Y. Ying, *Nature* **389**, 704 (1997).
6. P. D. Yang, T. Deng, D. Y. Zhao, P. Y. Feng, D. Pine, B. F. Chmelka, G. M. Whitesides, and G. D. Stucky, *Science* **282**, 2244 (1998).
7. P. D. Yang, D. Y. Zhao, D. I. Margolese, B. F. Chmelka, and G. D. Stucky, *Nature* **396**, 152 (1998).
8. R. D. Miller, *Science* **286**, 421 (1999).
9. R. Leung, W. Fan, J. Silkonia, and H. J. Wu, USA Patent No. 6213746 (April 2001).
10. J. L. Hedrick, R. D. Miller, C. J. Hawker, K. R. Carter, W. Volksen, D. Y. Yoon, and M. Trollsas, *Adv. Mater.* **10**, 1049 (1998).
11. J. L. Hedrick, K. R. Carter, J. W. Labadie, R. D. Miller, W. Volksen, C. J. Hawker, D. Y. Yoon, T. P. Russell, J. E. McGrath, and R. M. Briber, *Abstr. Pap. Am. Chem. Soc.* **141**, 1 (1999).
12. M. R. Baklanov, *Proceedings of the IEEE* (New Orleans, Louisiana, 2001), 189.
13. S. Yang, P. Mirau, E. Reichmanis, J. N. Sun, and D. Gidley, *Abstr. Pap. Am. Chem. Soc.* **224**, U507 (2002).
14. S. Lin, J. T. Wetzel, K. A. Monnig, P. A. Winebarger, S. Jang, D. Yu, and M. S. Liang, *Advanced Metallization Conference Proc.* (Montreal, Canada, 2001), 267.
15. A. M. Padovani, L. Rhodes, L. Riester, G. Lohman, B. Tsuie, J. Conner, S. A. B. Allen, and P. A. Kohl, *Electrochem. Solid State Lett.* **4**, F25 (2001).
16. D. D. Burkey and K. K. Gleason, *J. Vac. Sci. Technol. A* **22**, 61 (2004).
17. A. Grill and V. Patel, *Appl. Phys. Lett.* **79**, 803 (2001).
18. A. Grill, *J. Appl. Phys.* **93**, 1785 (2003).
19. K. Buchanan, K. Beekmann, S. Burgess, and J. Macneil, *Semiconductor Equipment and Materials International* (2002).

20. Y. H. Ye, S. Badilescu, and V.-V. Truong, *Appl. Phys. Let.* **81**, 616 (2002).

21. N. D. Denkov, O. D. Velev, P. A. Kralchevsky, I. B. Ivanov, H. Yoshimura, and K. Nagayama, *Nature* **361**, 26 (1993).

22. S. H. Park, D. Qin, and Y. Xia, *Adv. Mater.* **10**, 1028 (1998).

23. A. vanBlaaderen, R. Ruel, and P. Wiltzius, *Nature* **385**, 321 (1997).

24. B. K. Wang, M. J. Loboda, G. A. Cerny, R. F. Schneider, J. A. Seifferly, and T. Washer, *IEEE Interconnect Tech. Conf. Proc.* (Piscatawy, NJ, 2000) **277**, 52.

25. M. L. Hitchman and K. F. Jensen, *Chemical Vapor Deposition, Principles and Applications* (Academic Press, New York, 1993).

26. S. M. Gates, *Chem. Rev.* **96**, 1519 (1996).

27. N. Selamoglu, J. A. Mucha, D. E. Ibbotson, and D. L. Flamm, *J. Vac. Sci. Technol. B* **7**, 1345 (1989).

28. P. A. Coon, P. Gupta, M. L. Wise, and S. M. George, *J. Vac. Sci. Technol. A* **10**, 324 (1992).

29. H. G. Pryce Lewis, D. J. Edell, and K. K. Gleason, *Chem. Mater.* **12**, 3488 (2000).

30. T. Kelen, *Polymer degradation* (Van Nostrand Reinhold Co., New York, 1983).

31. H. G. Tomkins and W. A. McGahan, *Spectroscopic Ellipsometry and Reflectometry: A User's Guide* (Wiley-Interscience, New York, 1999).

32. M. Bass, E. W. Van Stryland, D. R. Williams, and W. L. Wolfe, *Handbook of Optics, Volume II Devices, Measurements and Properties* (McGraw-Hill, New York, 1995).

33. L. Peters, *Semiconductor International* (May 2002).

CHAPTER FIVE

Chemical Vapor Deposited Nanocomposites Fabricated Via Ultrasonic Atomization

A. D. Ross and K. K. Gleason

ABSTRACT

Composite thin films were created by a novel technique employing ultrasonic atomization to introduce the particles into the vacuum chamber during plasma-enhanced deposition of a matrix material. Co-deposition was confirmed by both fluorescent microscopy and FTIR analysis. Particle deposition was explored in the context of solvent properties as well as reactor conditions and the results were examined in the context of the calculated mass drying rate and droplet lifetime. The rate of solvent drying was determined to control how the particles are dispersed within the matrix, with reactor pressure and solvent choice have large influences. This technique could extend the CVD to applications currently possible only using wet processing techniques or multi-step processing.

5.1 INTRODUCTION

Nanocomposite thin films have numerous applications, including optoelectronic devices,[1,2] photonoic devices,[3] protective coatings,[4] electrocatalysists,[5,6] photovoltaic cells,[7] high-k dielectrics,[8] optical isolators,[9,10] sensors,[11-17] ferromagnetic composites,[18] electrodes,[19] and various electrical and optical applications.[20,21] A majority of these materials are fabricated using wet processing techniques. Chen et. al. fabricated thin films of nanocomposite dielectric gate insulator by dispersing titanium dioxide nanoparticles in organic solvent, and using spin-coat processing. After curing steps the matrix solidifies forming a cross-linked poly-4-vinylphenol polymer and with suspended titanium dioxide particles and the dielectric constant was controlled by varying the relative amounts of matrix and particles.[8] This type of material cannot currently be fabricated using a gas-phase, vacuum technique and these wet processes have several disadvantages, primarily with environmental, health, and safety issues. They require the use of a solvent to distribute the polymers and often a subsequent rinsing step, both of which have significant waste and can expose workers to chemicals and out-gassing. Additionally, wet processes are often limited by the solubility of polymers and problems can occur for composite materials with aggregation of particles.

Chemical vapor deposition (CVD) is a more environmentally friendly manufacturing method commonly used for thin film deposition.[4,22] CVD utilizes gas phase chemistries in a low to ultra-low pressure environment to produce well-defined, high quality films in a controllable and tunable fashion.[23] There is limited worker chemical exposure and no waste solution. However, when creating materials via CVD there are complications in depositing two separate components simultaneously, which has limited its extendibility into the manufacturing of

composite thin films. Often, CVD might be advantageous in producing one or more of the desired composite components, but is unable to either created the particle component, such as when using metal particles, or unable to do so simultaneous with the matrix deposition. Wang and Swain used a multi-step process of wet-steps and CVD to produce platinum and diamond composite materials, first by depositing diamond onto a substrate using microwave-assisted CVD, then removing the substrate from vacuum and electrodepositing metal particles from a solution, then returning the substrate to the reactor for further diamond deposition to cover the platinum.[5,6] This complicated and multi-step process could be streamlined if reduced to a single CVD processing step.

Two different processes possibilities exist for the production of composite, or dispersion, coatings using solely CVD.[4] One option occurs when precursors for both the particle and matrix components are introduced to the reactor and simultaneously undergo reactions leading to the formation of separate phases. This process has proved challenging since the deposition conditions for both the particle formation as well as the matrix must coincide, often leaving only a small window and producing non-optimal properties for one or both of the components.[24] Additionally, this process requires both the matrix and particle precursors to have certain volatilities.

To avoid the need to have compatible processing windows for both phases, an alternate concept is to produce composite dispersion coatings by simultaneous depositions of particles during the CVD process by injection into the gas phase, having the advantage that any type of particle could be incorporated. Additionally, if no modifications of the particles are needed, the CVD processing conditions can be chosen such that the optimal properties for the matrix material are achieved. This work explores the use of an ultrasonic atomizer to distribute particles during plasma-enhanced CVD for the creation nanocomposite thin films. Atomization of

liquids into vacuum chambers has previously been used to aid in introducing non-volatile substances (Leiby, Sono-Tek Corporation).

Aqueous solutions of dextran, ethylene glycol solutions of dextran, and aqueous suspensions of polystyrene nanospheres were the three types of particles used for the depositions. Dextrans are hydrophilic polysaccharides having high water solubility, low toxicity and relative inertness. These properties make dextrans effective water-soluble carriers for dyes, indicators and reactive groups in a wide variety of applications. Attachment of a fluorescent dye to the dextran molecule allows for direct observation of the distribution of the particles within the matrix using simple microscopy technique. Polystyrene nanospheres were also used as particles in the composite material and their larger size allowed viewing via SEM.

Pulsed plasma-enhanced CVD of organoisilicon precursors is used to create methyl doped silicon dioxide, or an organosilicate glass (OSG). OSGs are a common used matrix material in composite thin films.[5,25,26]

5.2 Experimental

Depositions were carried out in a custom-built, parallel-plate vacuum chamber shown in Figure 5-1.

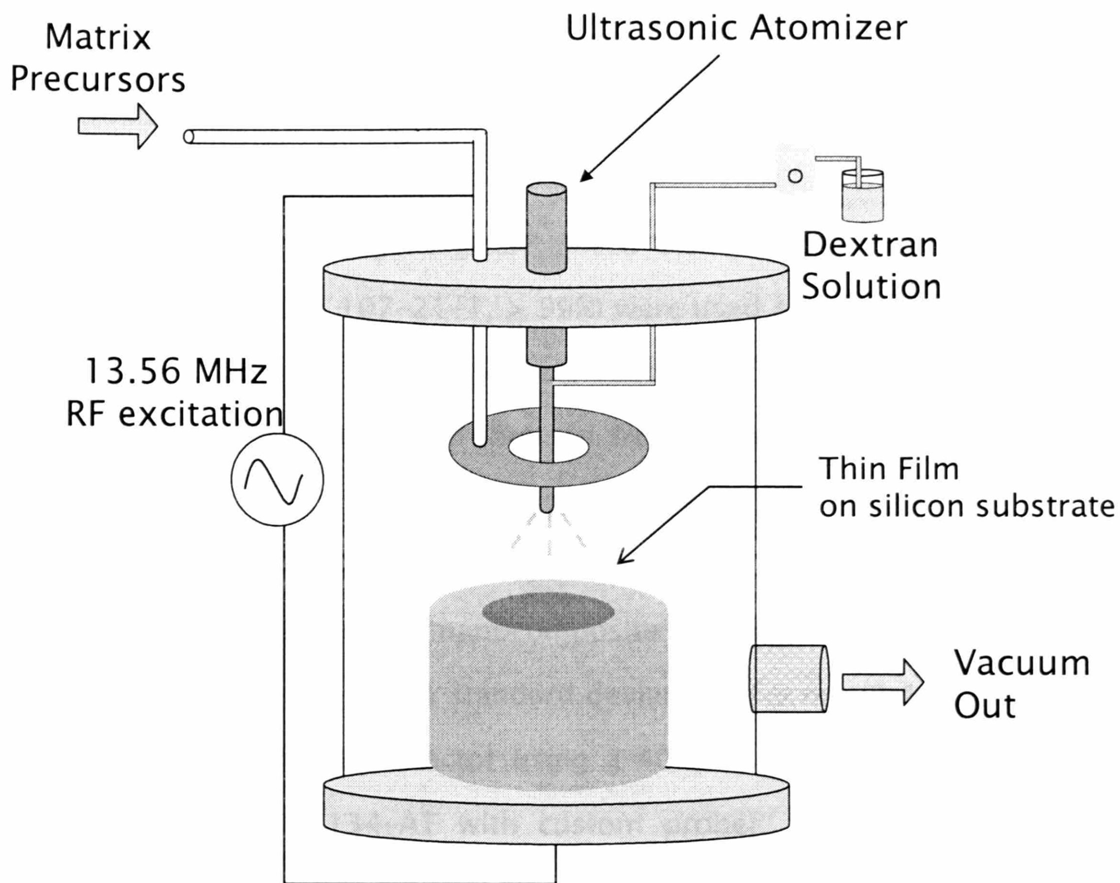

Figure 5-1: Reactor configuration of simultaneous plasma-enhanced deposition of matrix material and ultrasonic atomization deposition of particles.

The PECVD system has an upper electrode powered by a 13.56 MHz RF source (ENI HF650) with attached matching network (Heathkit SA2060-A) and a grounded lower electrode. The lower electrode also functions as the substrate stage. The substrates used were 100mm diameter silicon wafers. The upper electrode / shower-head distributes the matrix precursor gases over the substrate. Tetraethoxysilane (TEOS, Gelest Inc., CAS 78-10-4, > 99%) was the monomer used for matrix fabrication with no further purification. The TEOS was volatilized in a glass jar and delivered to the reactor chamber via the showerhead through a MKS M100B mass flow controller at a rate of 2 sccm. Oxygen was delivered at a rate of

12 sccm to the reactor via the showerhead using a UNIT Instrument URS-100 Mass Flow controlling system. The plasma was pulsed at a 10-40 ms on-off rate with a peak power of 300 W.

Water (deionized, Reagent grade, Ricca Chemical Company) and Ethylene Glycol (Sigma Aldrich, CAS 107-21-1, > 99%) were used as solvents for the dextran particle solution. Dextran with fluorescent Texas Red® labeling (absorbs 595 nm, emits 615 nm) and 3000 MW was obtained from Molecular Probes and solutions were made with a concentration of approximately 0.01 mg/ml. Additionally, polystyrene nanospheres (Interfacial Dynamics) in an aqueous suspension were used as particles to fabricate the nanocomposite thin films. The nanospheres have a mean diameter of 96 nm with a standard deviation of 9 nm (9.4 %). The particle solution was delivered to the reactor using a 40 kHz ultrasonic atomizer (Sonics and Materials, model VC134-AT with custom probe). The atomizer uses low ultrasonic vibrational energy for atomization, avoiding the addition of extra gases often used to shear fluid into droplets and allowing the desired reactor conditions to be maintained. The converter is place through a 1-1/4" quick-disconnect flange on the reactor lid and the probe extends through a centered ½" opening in the showerhead. A small peristaltic pump feeds the particle solution at a rate of approximately 0.2 ml/min into the vacuum chamber by passing it through the reactor lid and into an aperture above the atomizing probe. When the solution reaches the probe tip, it is dispersed into 45 μm diameter droplets. The solvent in the droplets then evaporates as they descend toward the substrate.

For all depositions, chamber pressure was maintained at between 100 and 500 mTorr, and is controlled by a butterfly valve (MKS 253B) connected to an MKS model 651C exhaust valve controller. Thermal annealing was completed at temperatures of 400 °C and ambient pressure in a nitrogen atmosphere for one hour.

Fourier Transform Infrared (FTIR) Spectroscopy was performed on a Thermo Nicolet Nexus 870 ESP spectrometer in transmission mode at 4 cm^{-1} resolution using 64 scan averaging. A 10 minute nitrogen purge was performed between each measurement to diminish the effects of carbon dioxide and moisture. All spectra were baseline corrected. Fluorescence microscopy was performed using is Axiovert 135 inverted microscope running Openlab software. Scanning electron micrograph (SEM) and was performed on a JEOL 6320FV.

5.3 Results and Discussion

Composite materials were created by simultaneous pulse-plasma enhanced CVD of tetraethoxysilane (TEOS) with oxygen and ultrasonic atomization delivery of an aqueous solution of fluorescent dextran. The TEOS precursor combines with oxygen combine to form a matrix of methyl doped silicon dioxide, or organosilicate glass (OSG). Figure 5-2 shows the fluorescent microscopy picture of a composite film, taken at an absorbance of 615 nm. Brighter spots clearly signify areas were the dextran was deposited within the matrix.

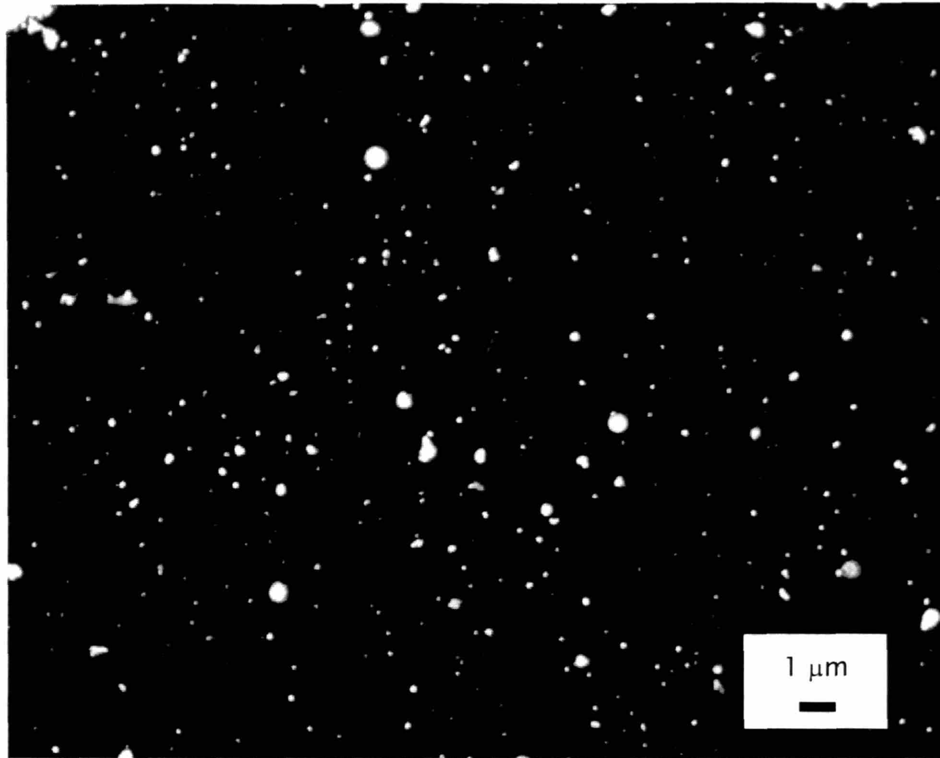

Figure 5-2: Fluorescent microscopy of composite thin films consisting of OSG matrix and fluorescently labeled dextran particles.

These spots could represent either single dextran molecules or nanocrystals of dextran. The latter could form when as the solvent in the droplet evaporates. The maximum crystal size is determined by the size of the droplet, here 45 μm in diameter, and concentration of the dextran in the solution. For the highest concentrations used in this study, up to 10^5 dextran molecules could be in each atomized droplet. Therefore, the larger bright spots seen in the pictures could indicate either the crystallization of dextran particles due to high solution concentrations or increased, uneven density of fluorescent tagging within dextran. Figure 5-3 shows the FITR spectra of (a) the fluorescent dextran particles, (b) the OSG matrix, and (c) composite material.

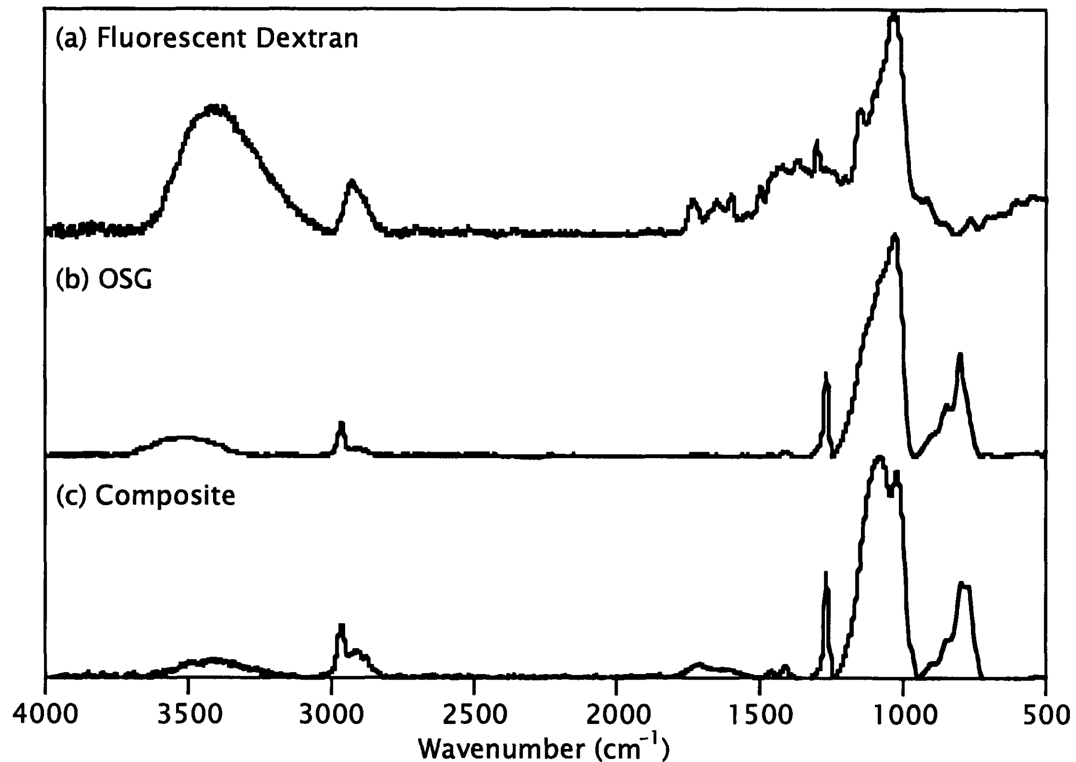

Figure 5-3: FTIR spectra of (a) pure fluorescently labeled dextran (b) pure OSG matrix material and (c) the composite material.

The fluorescent dextran spectrum has distinguishable peaks showing hydroxyl incorporation (3000-3700 cm^{-1}), methyl groups (2800-3000 cm^{-1}), and ring stretches (1000-1200 cm^{-1}). Additionally, there are a multitude of unresolved peaks between 1250 and 1800 cm^{-1}, most likely due to the fluorescent tagging. The OSG spectrum shows matching peaks for the hydroxyl groups (3000-3700 cm^{-1}) and methyl groups (2800-3000 cm^{-1}), as well as an overlapping peak between 1000-1200 cm^{-1}, signifying the signature Si-O-Si peak of a silicon dioxide polymer backbone. For the co-deposition spectrum, all of the common and overlapping peaks for the dextran and OSG are visible, as well as the peaks between 1500 and 1850 cm^{-1} belonging exclusively to the dextran, reconfirming that a composite material was produced.

Both the reactor conditions and the solvent choice greatly influence the dispersion of the dextran during of the deposition. It is desirable that minimal solvent evaporates as the particle solution traverses to the atomizer tip to maintain the initial expected concentration of particles; this favors a solvent with a low volatility. However, it is also imperative that the solvent is volatile enough to fully evaporate before striking the substrate surface, which favors a solvent with a low volatility. An analysis was performed by examining the effects of solvent volatility and reactor pressure for an evaporating droplet of pure solvent. This case was considered because only dilute concentrations of the particle solutions or suspensions were used and hence the droplet is composed of primarily of solvent. Thus, it is informative to consider the simple case of the drying dynamics of a pure solvent droplet. The droplet evaporates and reduces in size as the solvent volatizes from the surface of the droplet into the surrounding low pressure gas phase. For a droplet size less than the mean free path of the solvent in the gas phase, the mass rate of evaporation, I, and lifetime for an evaporating spherical drop, t, are given by the following equations[27,28]

$$I = \frac{2\pi D_v M d_p (p_d - p_\infty)}{RT} \quad (5\text{-}1)$$

$$t = \frac{R \rho_p d_p^2 T}{8 D_v M (p_d - p_\infty)} \quad (5\text{-}2)$$

where D_v is diffusion coefficient of the solvent in a gas phase of pure solvent, M is molecular weight of the solvent, d_p is droplet diameter, p_d is the partial pressure at the drop's surface, p_∞ is the partial pressure of solvent in the reactor, ρ_p is the density of the drop liquid, T is the temperature, and R is the gas constant. For our system, the vapor pressure at the droplet surface is simply the saturation

pressure of the solvent at the given temperature. The driving force for evaporation rate is the difference in the saturation pressure from the partial pressure of solvent in the reactor. The variables T, p_∞, and p_d are a function of the reactor conditions, while M, D_v, ρ_p, and p_d are function of the solvent. This case represents the diffusion limited model, for droplet greater than 1 μm in diameter. It is also assumes that the partial pressure at the surface of the drop, or the vapor concentration at the surface, equals the saturated vapor pressure at the droplet temperature. These equations also assumes constant temperature and do not take into account temperature depression with evaporation. Toward the end of drying after significant portions of the solvent have evaporated, the added non volatile particles become highly concentrated and the evaporation would exhibit non-ideal behavior,[28] which is not captured by these equations.

Table 5-1 shows the relative drying rates, calculated using Equation 5-1, under vacuum conditions for 45 μm diameter droplets of solutions of water and ethylene glycol at 5 different volume fractions. The saturation vapor pressures given in the table indicates the relative volatility of the different solutions, with pure water being the most volatile. Depositions using water were performed at higher reactor pressure, which decreases the evaporation driving force, due a limitation in pumping capabilities. Even with a higher pressure, the water evaporates more quickly due to its higher volatility which leads to a higher evaporation driving force. The pure ethylene glycol solution does not evaporate at the given conditions since its saturation vapor pressure is approximately equal to the reactor pressure, resulting in zero driving force.

Table 5-1: Effect of solvent on evaporation rate of droplets

% Volume Ethylene Glycol	Psaturation (298K) (Torr)	Reactor Pressure (Torr)	Relative Rate
0	23.34	0.5	1.00
80	10.92	0.1	0.57
90	8.86	0.1	0.55
95	3.64	0.1	0.24
100	0.56	0.1	0.03

These calculations are corroborated by the corresponding pictures from fluorescent microscopy shown in Figure 5-2 and Figure 5-4. For the pure ethylene glycol, the drop size appearing on the picture is approximately 45 μm, which is equivalent to the drop produce by the atomizer indicating negligible evaporation. Increasingly smaller drop sizes are seen as the volatility of the solution increases and the evaporation rate improves.

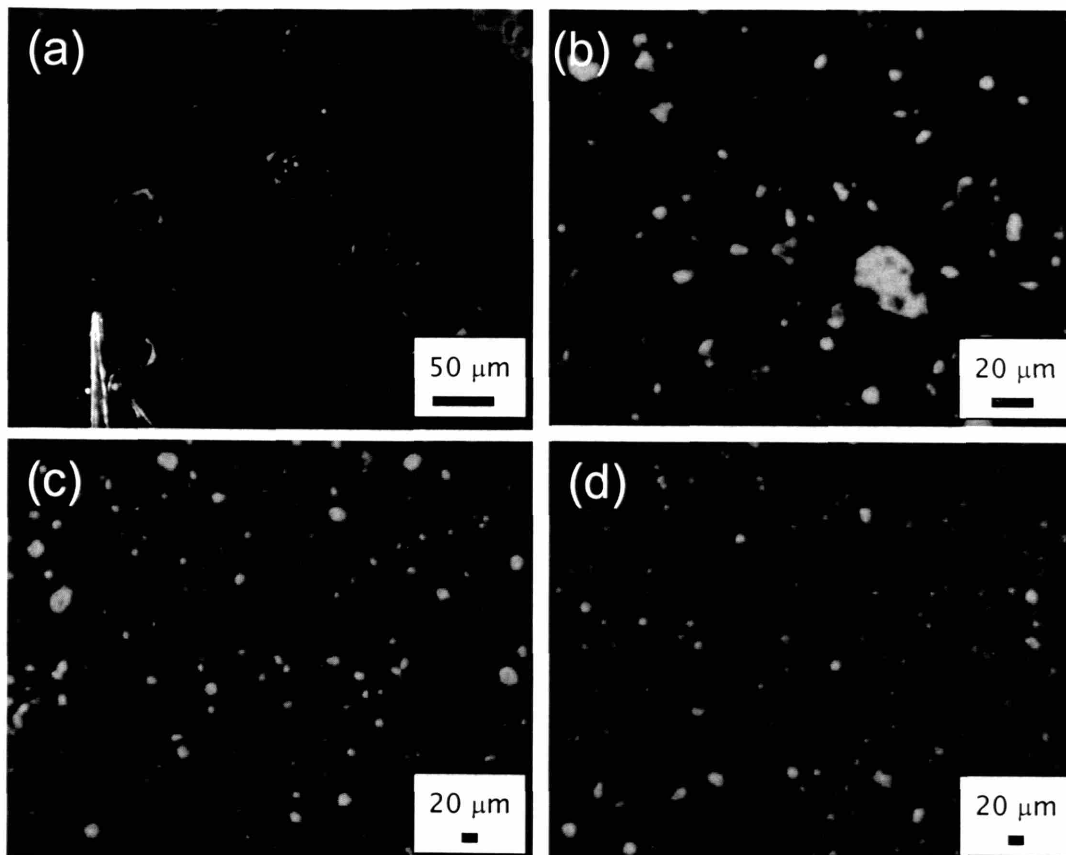

Figure 5-4: Fluorescent microscopy of composite OSG films with labeled dextran where the later was delivered by ultrasonic atomization from aqueous solutions of varying ethylene glycol content (a) 100% (b) 95% (c) 90% and (d) 80% ethylene glycol. The volatility of the solvent greatly effects the particle deposition. The pure ethylene glycol has a comparatively low volatility, and does not evaporate before striking the substrate. Water, with a much higher volatility, evaporates quickly leaving only the dextran crystals to descend onto the substrate.

The reactor pressure also affects the driving force for the rate of evaporation and drying time. Figure 5-5 shows the calculated droplet lifetime and driving force versus reactor pressure. As the reactor pressure approaches the solvent's saturation pressure, the driving force approaches zero and the droplet lifetime increases exponentially.

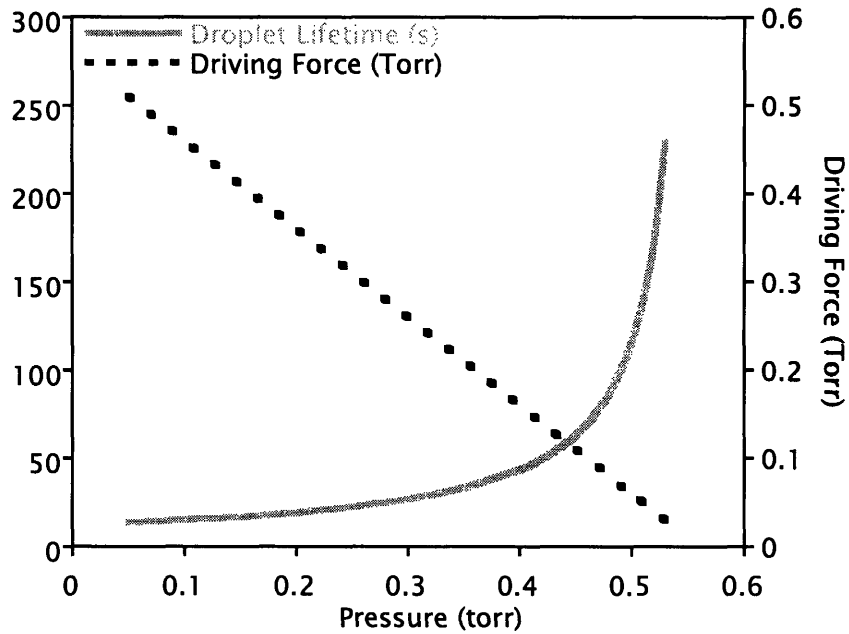

Figure 5-5: Calculated effect of reactor pressure on the droplet lifetime of ethylene glycol.

Figure 5-6 shows fluorescent microscopy dextran deposition using an ethylene glycol solvent at two different pressures (performed at slightly elevated temperatures from previous).

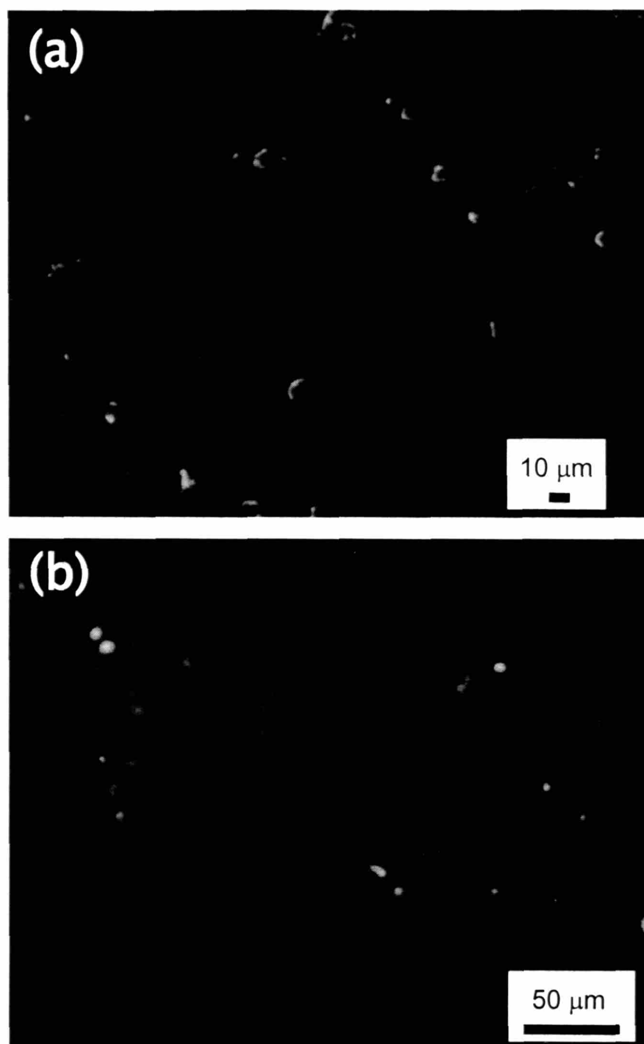

Figure 5-6: Fluorescent microscopy of OSG films with labeled dextran where the ultrasonic atomization of the dextran employed 100% ethylene glycol at (a) 150 mTorr and (b) 500 mTorr. The evaporation driving force is fueled by the difference in the solvent saturation pressure and reactor pressure, and as the reactor pressure increases to 500 mTorr and approaches the saturation pressure, no solvent evaporation occurs and the droplets strike the substrate with their original diameter of 45 μm.

The distance between atomizer tip and substrate as well as the velocity of the droplet determine at what stage in the drying process the droplet or particles will reach the substrate. The diameter of the drops hitting the surface for the lower pressure of 150 mTorr are around 10 μm while those at the 500 mTorr pressure are

40-50 μm in diameter. As predicted by Figure 5-5, the droplet lifetime is shorter and evaporation faster at lower pressures so the droplet diameter decreased significantly before striking the substrate. However, at 500 mTorr, no significant evaporation occurred prior to hitting the substrate.

Another extension of composite materials removes the dispersed particles by thermally decomposition, leaving behind only the matrix and resulting in a porous, void structure. The composite sample detailed in Figure 5-2 and Figure 5-3 was annealed at 400 °C and the resulting FTIR and fluorescent microscopy are shown in Figure 5-7.

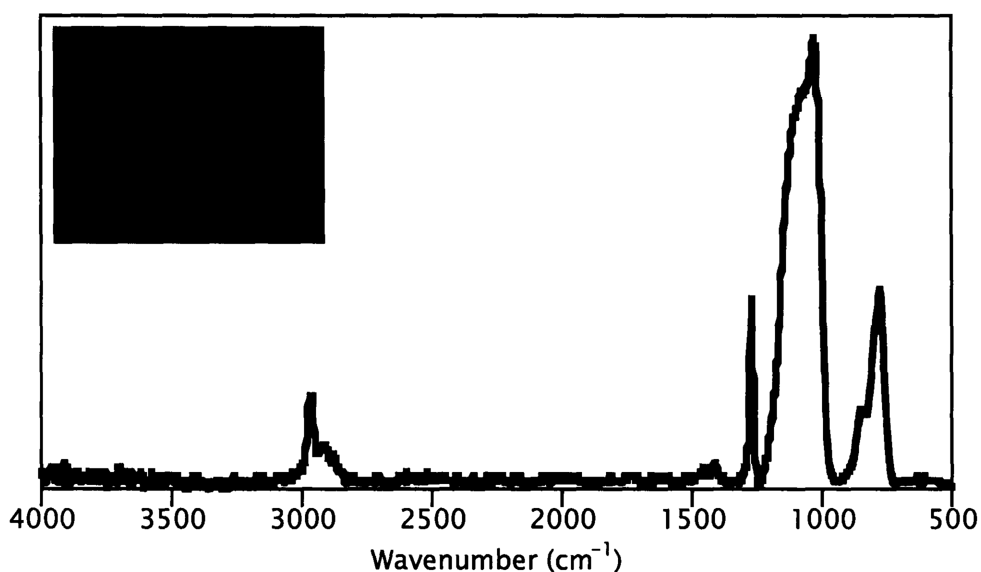

Figure 5-7: FTIR spectra of annealed composite thin film and (inset) fluorescent microscopy of annealed films. Both indicate removal of dextran particles.

The microscopy shows visually the removal of the particles and the absence of the peaks between 1500-1850 cm^{-1} in the FTIR spectrum confirms the removal. Providing a sufficiently strong matrix is created, this process can result in the fabrication of a porous thin film.

Ultrasonic atomization depositions can be applied to both small and large scale nanocomposites. Polystyrene nanospheres, with 96 nm diameters, were deposited in alternating layers with an OSG matrix. This composite material was then annealed, decomposing the polystyrene and creating a void structure. Figure 5-8 shows an SEM image of the resulting porous structure. The darker spherical holes indicate where the polystyrene nanospheres were deposited into the matrix before removal. One advantage to this synthesis of porous materials with this method is that the particles and matrix are not covalently bonded, resulting in negligible disruption of the matrix upon particle decomposition.

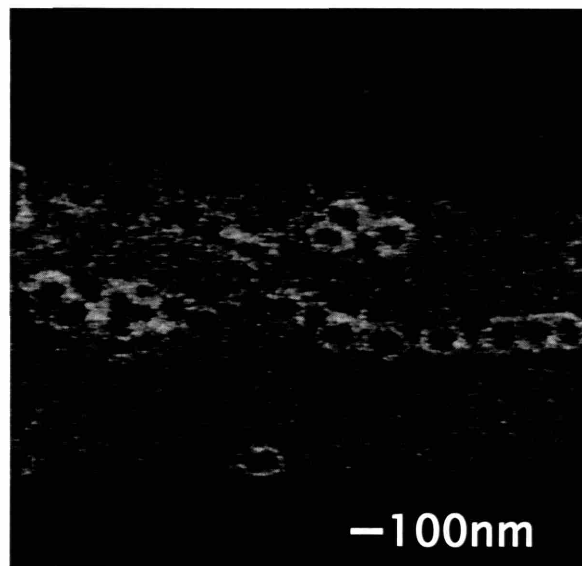

Figure 5-8: SEM image of porous OSG matrix structure with 96nm pores, originally a composite film with polystyrene microbeads.

5.4 CONCLUSIONS

Composite thin films were created by a novel technique employing ultrasonic atomization to introduce the particles into the vacuum chamber during plasma-enhanced deposition of a matrix material. Fluorescent microscopy and FTIR

analysis confirmed co-deposition. Particle deposition was explored in the context of solvent properties as well as reactor conditions by examining their effect on the mass rate loss of evaporation and droplet lifetime. The rate of solvent drying determines the dispersion of the particles and the drying rate can be experimental controlled by varying the reactor pressure and changing solvents, with fine tuning achieved through solvent mixtures. This technique could extend the CVD technique to applications currently possible only using wet processing techniques or multi-step processing. Farooq and Hutchins produced metal-dielectric graded index solar selective coating in which the metallic volume changed with depth of the coating by doing multi-layer coatings with numerous sputtering depositions. Multilayer processes such as this are not possible using spin-on techniques, since the solvents used in deposition of the subsequent layers would dissolve initial ones. By adjusting the relative feed rates of matrix precursors and particle solution to the reactor during depositions, graded films could be produced in one processing step using particle atomization with chemical vapor.[29]

Another important result is that the fluorescent functionality of the dextran remained intact during the co-deposition process, extending the scope of the method to include composites where particle structure is complex and must remain intact. Plasma pulsing could have contributed, since it allows a period when any modification of the particle is minimal or non-existent. Sensors are a common application of thin films and often require specific functionality. Thin films with distinctively functionalized cyclodextrins are used in sensor and cantilever manufacturing,[14-16] where the ability of the cyclodextrin to maintain the desired chemical structure is crucial to maintaining the device performance. Atomization delivery would keep intact the chemical structure of the cyclodextrin while imbedding it in a matrix material. Additionally the use of fluorescent dyes and

particles entrapped within a matrix has application in sensors,[11,12] and fabrication using CVD has been shown feasible this technique.

REFERENCES

1. U. Sohling, G. Jung, D. U. Saenger, S. Lu, B. Kutsch, and M. Mennig, *J. Sol-Gel Sci. Technol.* **13**, 685 (1998).
2. D. U. Saenger, G. Jung, and M. Mennig, *J. Sol-Gel Sci. Technol.* **13**, 635 (1998).
3. M. Guglielmi, A. Martucci, E. Menegazzo, G. C. Righini, S. Pelli, J. Fick, and G. Vitrant, *J. Sol-Gel Sci. Technol.* **8**, 1017 (1997).
4. M. L. Hitchman and K. F. Jensen, *Chemical Vapor Deposition, Principles and Applications* (Academic Press, New York, 1993).
5. J. Wang and G. M. Swain, *J. Electro. Chem. Soc.* **150**, E24 (2003).
6. J. Wang, G. M. Swain, T. Tachibana, and K. Kobashi, *Abstr. Pap. Am. Chem. Soc.* **222**, U89 (2001).
7. K. Okajima, C. J. Wen, K. Kato, I. Sakata, and K. Yamada, *Electrochemistry* **67**, 248 (1999).
8. F. T. Chen, C. W. Chu, J. He, Y. Yang, and J. L. Lin, *Appl. Phys. Lett.* **85**, 3295 (2004).
9. L. Ba, L. D. Zhang, and X. P. Wang, *Solid State Commun.* **104**, 553 (1997).
10. N. Matsunami and H. Hosono, *Appl. Phys. Lett.* **63**, 2050 (1993).
11. Y. Sadaoka, Y. Sakai, and X. Wang, *J. Mater. Sci.* **29**, 883 (1994).
12. P. S. Grant and M. J. McShane, *IEEE Sens. J.* **3**, 139 (2003).
13. X. Yang, S. Johnson, J. Shi, T. Holesinger, and B. Swanson, *Sens. Actuator B-Chem.* **45**, 87 (1997).
14. B. Swanson, S. Johnson, J. Shi, and X. Yang, *ACS Symposium Series* (Washington, 1998) **690**, 130.
15. C. A. Tipple, N. V. Lavrik, M. Culha, J. Headrick, P. Datskos, and M. J. Sepaniak, *Anal. Chem.* **74**, 3118 (2002).
16. M. Culha, N. V. Lavrik, F. M. Schell, C. A. Tipple, and M. J. Sepaniak, *Sens. Actuator B-Chem.* **92**, 171 (2003).
17. Y. M. Lim, P. H. Kang, Y. M. Lee, and Y. C. Nho, *J. Indust. and Eng. Chem.* **10**, 267 (2004).
18. R. Ramprasad, P. Zurcher, M. Petras, M. Miller, and P. Renaud, *J. Appl. Phys.* **96**, 519 (2004).
19. J. Reyes-Gomes, J. A. Medina, K. M. Jeerage, W. A. Steen, and D. T. Schwartz, *J. of Electro. Chem. Soc.* **151**, D87 (2004).
20. B. Bhattacharjee, D. Ganguli, S. Chaudhuri, and A. K. Pal, *Mater. Chem. Phys.* **78**, 372 (2002).
21. P. M. Ajayan, L. S. Schadler, and P. V. Braun, *Nanocomposites Science and Technology* (Wiley-VCH GmbH & Co., New York, 2003).
22. L. Peters, *Semiconductor International* (May 2002).
23. R. D'Agostino, Plasma deposition, treatment, and etching of polymers (Academic Press, Boston, 1990).
24. D. D. Burkey and K. K. Gleason, *J. Appl. Phys.* **93**, 5143 (2003).

25. D. D. Burkey and K. K. Gleason, *J. Vac. Sci. Technol. A* **22**, 61 (2004).
26. A. Grill, *J. Appl. Phys.* **93**, 1785 (2003).
27. W. C. Hinds, *Aerosol Technology* (John Wiley & Sons, New York, 1982).
28. P. C. Reist, *Aerosol Science and Technology* (McGraw-Hill, New York, 1993).
29. M. Farooq and M. G. Hutchins, *Sol. Energy Mater. Sol. Cells* **71**, 523 (2002).

CHAPTER SIX

CONCLUSIONS & FUTURE DIRECTIONS

6.1 CONCLUSIONS

This thesis has presented a potential low-*k* dielectric material solution to address the interconnect delay problem stemming from microelectronic device miniaturization. Dense organosilicon films produced by pulsed plasma-enhanced chemical vapor deposition showed promise as low-*k* dielectrics, with dielectric constants below 2.8. Two different fabrication methods were presented for producing composite films, which can be thermally annealed to create porous OSG materials.

6.1.1 OSG MATRIX MATERIALS

The OSG matrix research was driven primarily by understanding structure-property-processing fundamentals, with mechanical integrity identified as a key issue for low-*k* integration. OSG thin films were deposited via pulsed plasma-enhanced CVD using two sets of precursor gases, diethylsilane with oxygen and octamethylcyclotetrasiloxane with hydrogen peroxide.

Diethylsilane was originally the chosen as the primary precursor due to its higher organic content than its methylsilane counterparts; however, the organic content can ultimately become the limiting factor if carbon bridging occurs and silicon carbide formation begins. Considerable hydroxyl inclusion led to condensation reactions upon annealing at 400 °C, resulting in a more crosslinked material with improved hardness and modulus. All films showed a modulus of 4.0 GPa or greater, indicating mechanical integrity would remain intact for a standard oxide CMP process.

Depositions using octamethylcyclotetrasiloxane employed a hydrogen peroxide oxidant for deliberate incorporation of silanol moieties and FTIR analysis

revealed successful hydroxyl incorporation in the as-deposited materials. Complete removal of the hydroxyl groups after annealing indicated condensation reactions occurred between proximal hydroxyl groups, leading to the formation of additional Si-O-Si linkages which improved the film's mechanical properties. Detailed FTIR analysis places the structure-hardness relationship within the framework of the continuous random network theory and a percolation of rigidity was observed at a connectivity number of 2.35-2.4.

By adjusting processing parameters for OSG depositions, films can be systematically tuned to have its specific properties; however, there is often a give-and-take between achieving a lower index of refraction and obtaining higher deposition rates.

6.1.2 Composite Materials

Creation of composite materials using an all-CVD method is something with which researchers have struggled. Complications often arise in determining overlapping deposition conditions for both phases. In this work, nanocomposite thin films were fabricated using two different techniques, both of which use pre-formed particles, such as polystyrene nanospheres or small dextran particles, to decouple the matrix and particle depositions. In the first method, nanosphere templates were constructed using evaporation-induced self-assembly of polystyrene particles. Subsequent PPECVD of OSG matrix material throughout the template followed by thermal annealing to decompose the polystyrene produced nanoporous thin films yielding porosities as high as 74% and dielectric constants as low as 1.4. While this technique was successful, its multi-step procedure, which includes a wet process, is unappealing. A second technique was developed that allowed co-deposition under vacuum of dextran particles and an OSG matrix, using

ultrasonic atomization delivery and PPECVD, respectively. Fluorescently-labeled dextran particles were used for easy identification of particle deposition through fluorescent microscopy. This fabrication technique extends the CVD to applications currently only possible using wet processing techniques or multi-step processing.

6.2 FUTURE DIRECTIONS

Creating an all-CVD process for the fabrication of composite films is an important advancement and has numerous potential applications worthy of further investigation. Thin films sensors often require composite materials with specific functionality. The ability shown here of the fluorescent dextran particles to maintain their structural functionality with atomizer delivery make this process a prime candidate for sensor manufacturing. Other potential applications of composite materials, as well as porous materials, include photonics, optical wave guides, electrocatalysists, and protective coatings.

The atomizer-adapted reactor configuration has several limiting factors upon which improvements could be made. Ideally, the particle solution would have a concentration that permitted a single particle per atomized droplet, minimizing any clumping and thereby controlling the thin film morphology. An atomizer operating at higher frequencies or a nebulizer (Sono-Tek Corporation and Sonaer) producing smaller drop sizes would increase the allowable concentration and thus the efficiency of particle inclusion. Smaller drop sizes would also lead to quicker evaporation of the solvent, extending the range of usable solvents to heavier ones. In addition, adding an array of atomizers would improve uniformity in particle distribution. To prevent the particle solution from evaporating before reaching the atomizer tip, an inert gas, such as argon, could be used to create a back pressure and quickly push the solution through the tubing to the atomizer tip.

APPENDIX A

REACTOR CONFIGURATIONS

The CVD reactor used had two basic configurations, one for standard OSG depositions and another for ultrasonic atomization assisted co-deposition. The basic reactor body remained the same for both, with only the lid and showerhead undergoing alterations. Both Figure A-1 and Figure A-2 show the reactor in the second configuration and identifies many of the major components.

The chamber is stainless steel vessel having several ports. The stainless steel chamber is an 8" diameter, 16" high vacuum system equipped with many small ports for pumping and diagnostics.

The pressure in the reactor is monitored by a pressure transducer (MKS Baratron 626A) and controlled through a PI feedback controller (MKS 651C) linked to a butterfly valve (MKS 253B). A thermocouple feedthrough is available for substrate or stage temperature monitoring. Interferometry is used to determine film thicknesses and growth rates *in situ*.

The basic showerhead is comprised of a stainless steel mesh (0.008"thck, 0.007" diameter holes, 9% open area) with a Teflon base and allows good dispersion of the incoming gas over the wafer. The flow rates of the incoming gases are controlled by mass flow controlling system (UNIT Instruments URS-100) while liquid and solid precursors were heated and controlled either by a needle valve or a mass flow controller (MKS M-100B). Both entered the reactor through the showerhead.

Another feature of this reactor will be electrostatic clamping of the wafer. This is achieved by negatively biasing the lower electrode/substrate stage. A thin insulating Kapton® tape covers the electrode, separating it from the substrate and creating a capacitor. This clamps the wafer to the stage and allows for backside helium cooling. Helium will be fed to a cut out area between the wafer and the stage, creating a positive pressure of helium (~10 Torr). Since heat transfer at low pressures is extremely poor, the positive pressure created by the helium under the

wafer will improve the heat transfer from the stage to the wafer. Helium was chosen because of its high thermal conductivity. Cooling water will be used for stage cooling. Alternatively, a heating plate can be placed on the stage if higher substrate temperatures are desired.

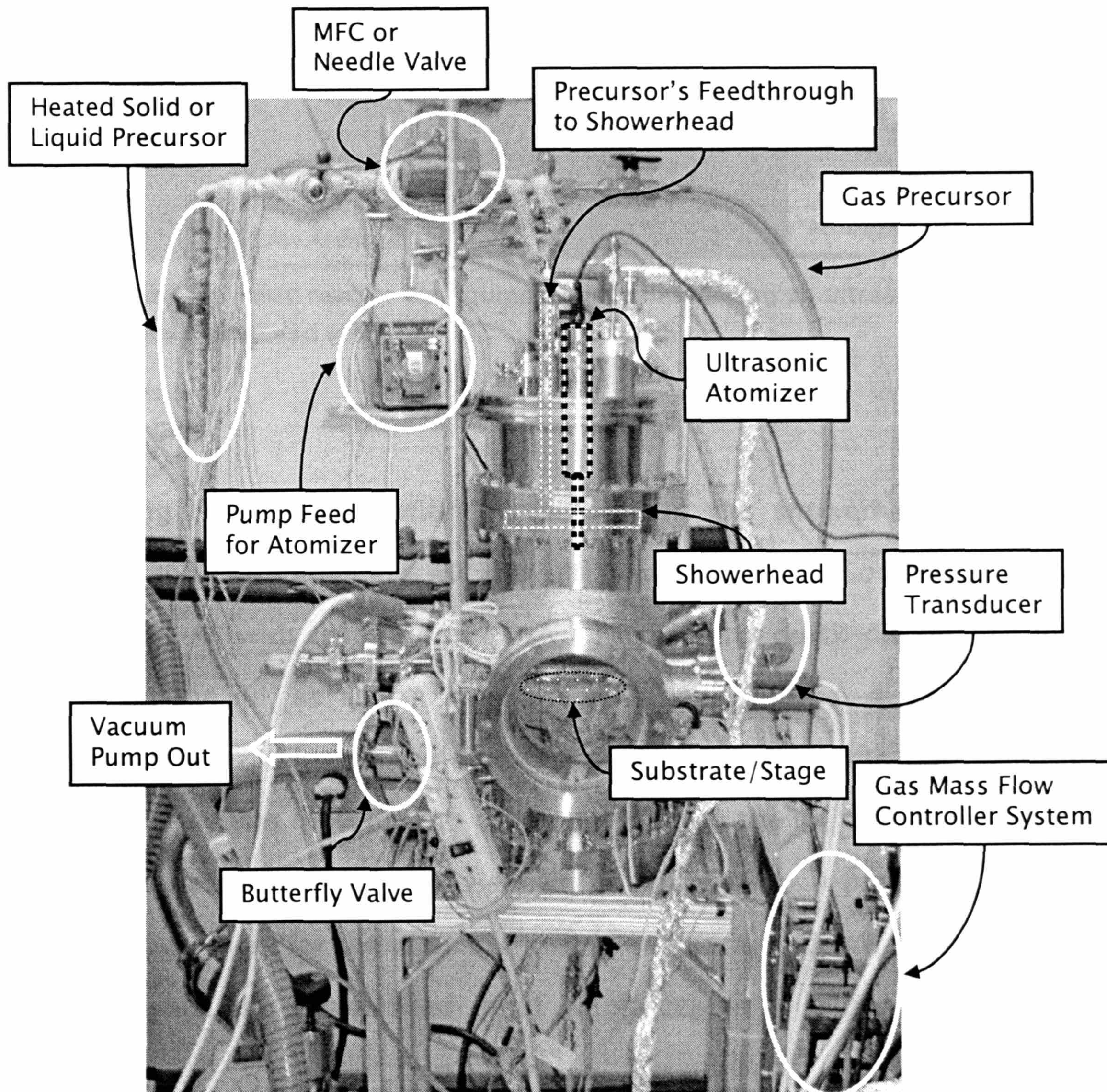

Figure A-1: Basic reactor configuration accommodating an ultrasonic atomizer.

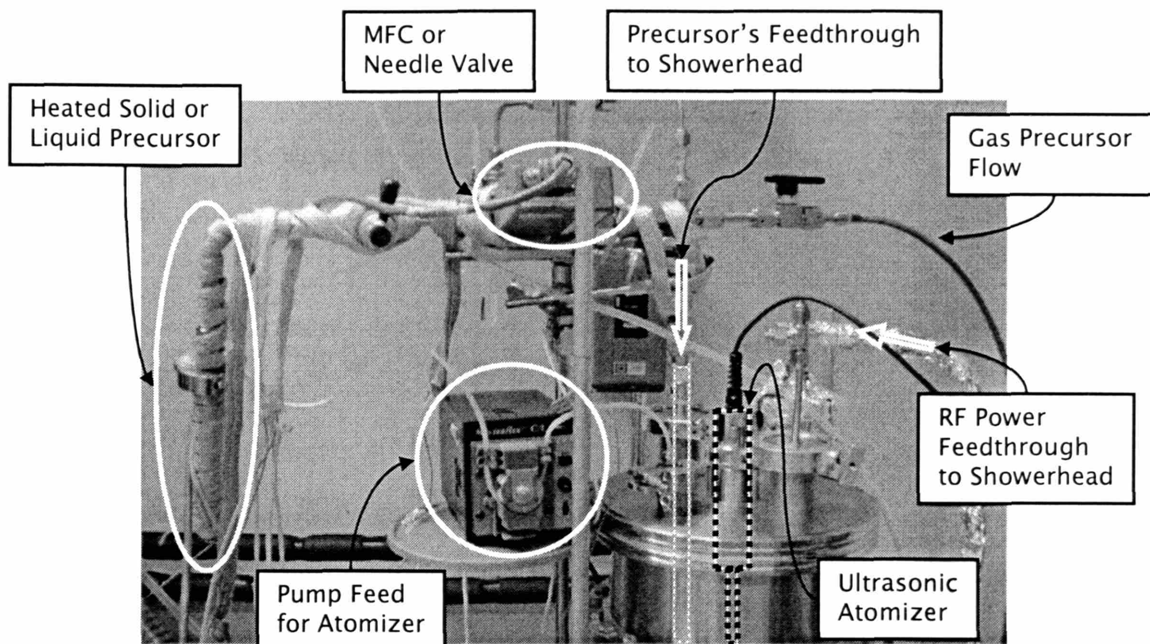

Figure A-2: Basic reactor configuration accommodating an ultrasonic atomizer, overhead view.

During the reconfiguration of the reactor, the showerhead and lid were redesigned to accommodate a 40 kHz ultrasonic atomizer (Sonics and Materials, model VC134-AT with custom probe). A 1 ¼" diameter quick-disconnect port was centered on the lid, as shown in Figure A-3 and Figure A-4, and clasped the atomizer converter, allowing the atomizer nozzle to extend into the reactor. The showerhead feed was moved to an off-center port on the lid, and consequently the showerhead was redesigned and is shown in Figure A-5. A centered ½" diameter opening allows room for the atomizer nozzle and spray to have a clear path to the substrate, while the showerhead input is off center to align with the lid feed through.

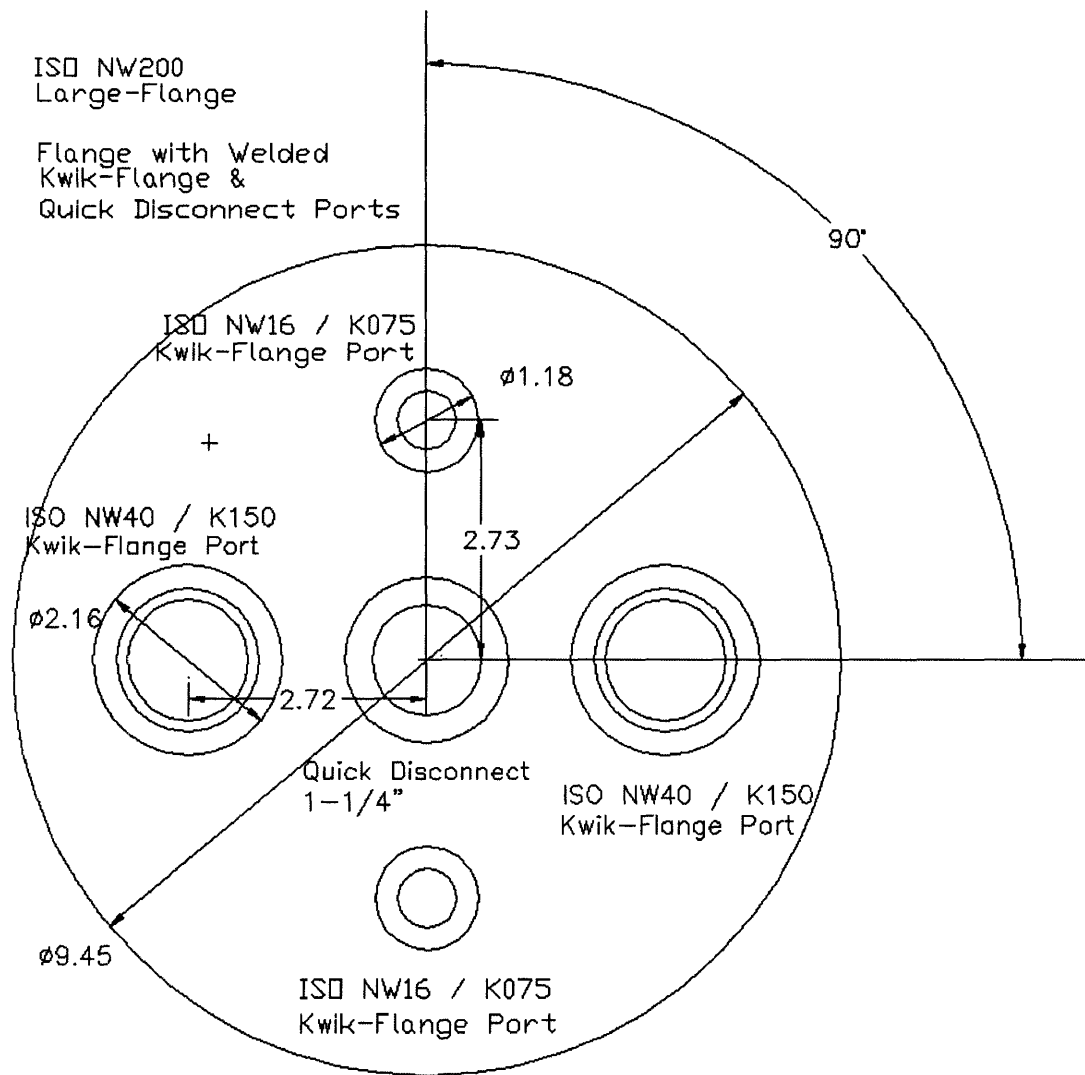

Figure A-3: CAD drawing of redesigned reactor lid accommodating ultrasonic atomizer (top view).

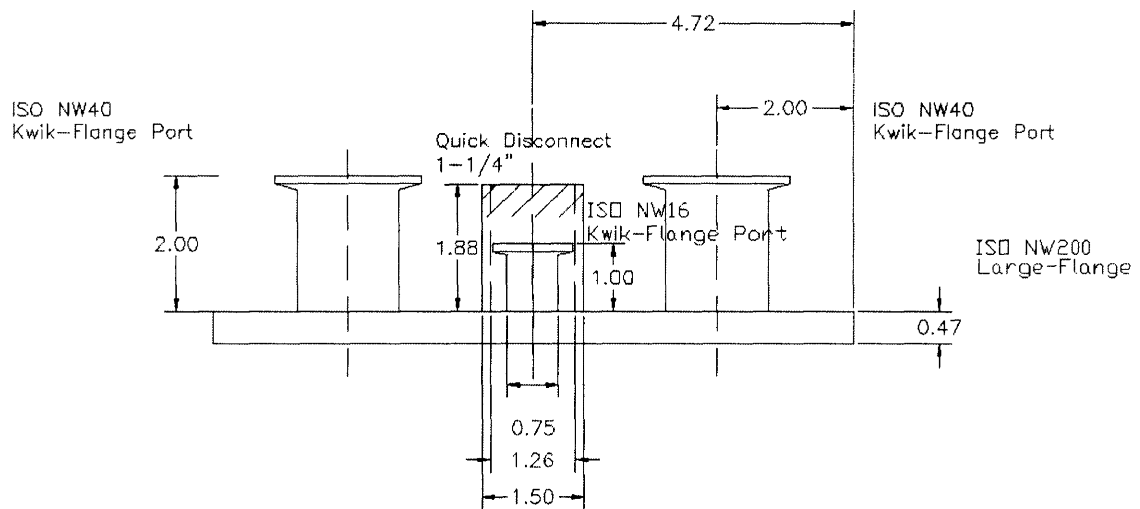

Figure A-4: CAD drawing of redesigned reactor lid accommodating ultrasonic atomizer (side view).

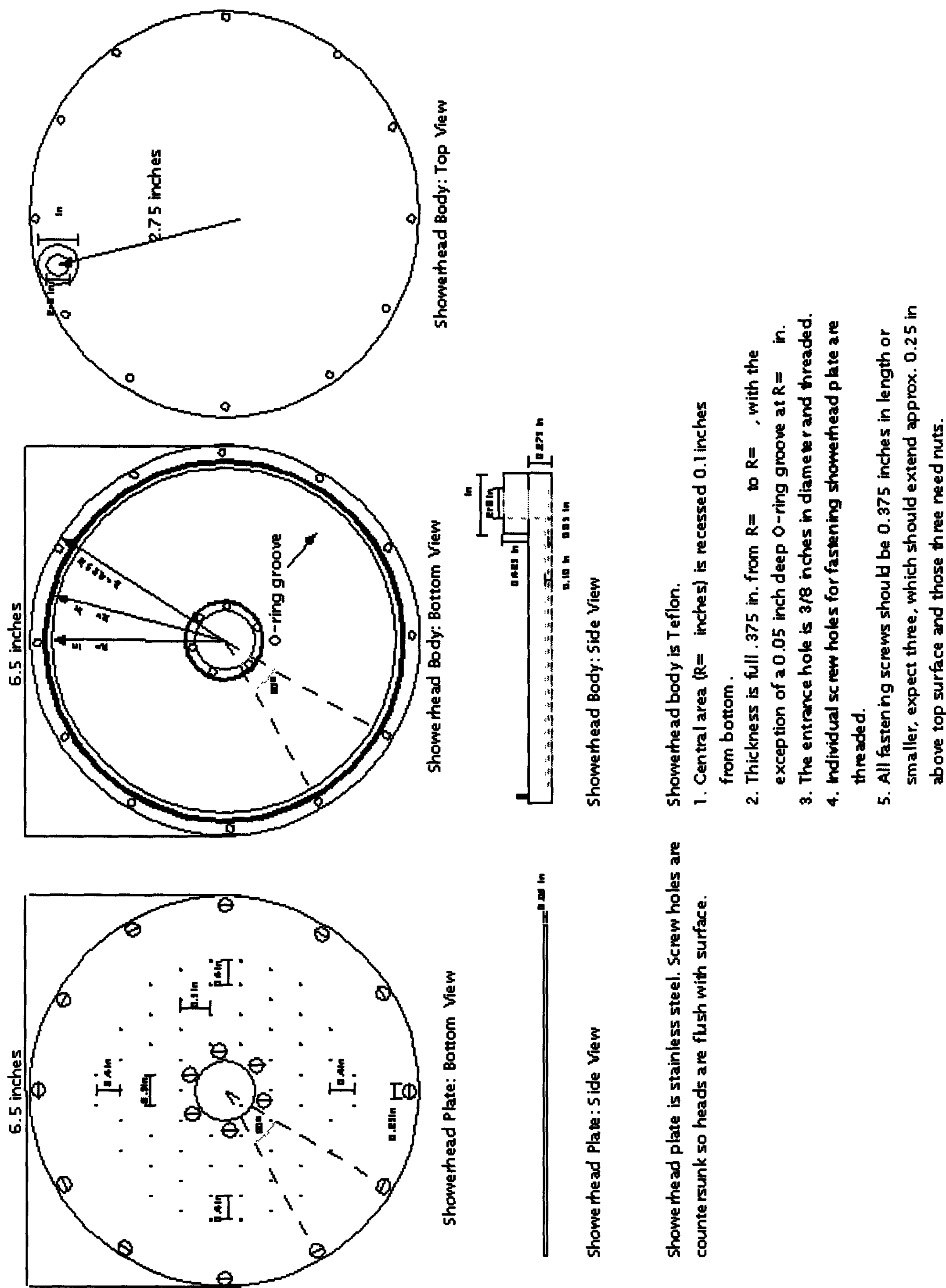

Figure A-5: Detailed drawing of redesigned showerhead accommodating ultrasonic atomizer.